Anisotropy of Transverse Relaxation in MRI of Articular Cartilage

M.Sc Thesis
Ville Kantola
University of Oulu
Faculty of Science
Biophysics Degree program
October 1, 2021
Supervisors:
Miika Nieminen
Jouni Karjalainen

Acknowledgements

I would like to express my gratitude for my supervisors Prof. Miika Nieminen and Ph.D Jouni Karjalainen. This thesis would not have been possible without their guidance, experience and knowledge. Additionally I would like to thank Prof. Kyösti Heimonen for their help and guidance during my studies, and Ph.D Victor Casula for their invaluable help with the thesis measurements.

A special thanks also goes to my friends and family for their support.

Contents

Symbols & Abbreviations

AC	Articular cartilage
B_0	Magnitude of the main magnetic field
DS	Deep segment containing the lower 50% of cartilage volume
ECM	Extracellular matrix
GAG	Glycosaminoglycan
gof	goodness of fit
G_F	Frequency-encoding gradient
G_P	Phase-encoding gradient
G_S	Slice-selection gradient
FOV	Field of View
k	Boltzmann constant
K	T_1 relaxation scaling constant
M_0	Magnitude of the total magnetisation
$M_{x,y}$	Transverse magnetisation
M_z	Longitudinal magnetisation
MRI	Magnetic Resonance Imaging
NMR	Nuclear Magnetic Resonance
MESE	Multi-Echo Spin-Echo
PCM	Pericellular Matrix
PG	Proteoglycan
r	Distance between two interacting dipoles
R_2	Transverse relaxation rate
$R_{2,a}$	Anisotropic component of R_2
$R_{2,i}$	Isotropic component of R_2
RF	Radio Frequency
ROI	Region of interest
RZ	Radial zone of articular cartilage
SE	Spin-Echo
SNR	Signal-to-noise ratio
SS	Surface segment containing the upper 50% of cartilage volume
SZ	Surface zone of articular cartilage
t	Time
T	Temperature
T_1	Longitudinal relaxation time
T_2	Transverse relaxation time
TE	Echo time

TR	Repetition time
TZ	Transitional zone of articular cartilage
γ	Gyromagnetic ratio
θ	Angle between the magnetic field and direction of organisation
μ_0	Vacuum permeability
ρ	Proton density
τ	Length of an RF-pulse
Δ	Phase angle
ω	Larmor frequency
$\hbar$	Reduced Planck constant

Abstract

The purpose of this M.Sc thesis was to study the anisotropic behaviour of transverse magnetic relaxation in articular cartilage using quantitative magnetic resonance imaging. Articular cartilage contains structures with a high degree of organization present in a predictable manner throughout the depth of the tissue, making it an interesting, albeit complex to model, candidate for anisotropy studies. The goal of the study was to use a transverse relaxation anisotropy model previously studied in an in vitro MRI study with a high-field research magnet, and attempt to employ this concept in a more clinical MRI setting using an ex vivo joint sample and a clinical MRI device. An additional goal of the study was to compare the transverse relaxation behaviour of cartilage obtained from different parts of an ex vivo joint sample.

The measurements consisted of a bovine stifle joint, consisting mostly of bone, soft tissue and cartilage, imaged in a 3 T clinical magnet. The imaging was performed using a large sampling of 30 unique sample orientations in relation to the main magnetic field, with angles of $5 - 10^{\circ}$ between each individual measurement. An image coregistration software was used to register all of the rotated images to a single geometry, allowing comparison of the measurements regardless of original measurement angle. Transverse relaxation time maps were created for each of the measurements from the corresponding coregistered images. Three regions of interest, two from femoral and one from tibial cartilage, were selected from the cartilage surfaces of the images and separated further into depth-wise sub-segments. In order to accurately rotate the large sample between measurements, a 3D printed rotation platform was additionally designed and constructed for the study.

This study showed that the anisotropy model previously used in studies with small cartilage samples and high field-strength MRI can be applied in a more clinical setting using a large ex vivo sample and a clinical MRI device. The relaxation rates obtained by fitting the established anisotropy model to the data obtained from the measurements followed this model remarkably well. Both the isotropic and anisotropic components of the relaxation rate model could be defined for each studied cartilage region. In the surface segment of cartilage the isotropic and anisotropic components showed little difference, while in the deeper cartilage the anisotropic component was found to be $2-7$ times larger than its isotropic counterpart. The sizes of the selected regions of interest were also shown to affect the values of the fitted anisotropy models, where an increase in region size corresponded with lower values for both isotropic and anisotropic fitting components.

1 Introduction

The purpose of this thesis is to study the transverse relaxation anisotropy and magic-angle effect in articular cartilage in a clinical 3 T magnetic field. The measurements were performed using quantitative magnetic resonance imaging (qMRI). The aim of qMRI studies is to perform the measurements in such a way, that the obtained parameters depend only on the physical properties of the imaging object instead of, for example, on the imaging sequence used. Some notable qMRI parameters that can be obtained in this way are the longitudinal and transverse relaxation times T_1, $T_{1\rho}$ and T_2.

By definition, anisotropic tissues contain a highly organized and orientation dependent internal structure. Commonly studied anisotropic tissues include tendons, white matter, peripheral nerves, cartilage and certain types of muscle tissue [1, 2, 3]. Articular cartilage (AC) is one such tissue, containing a complex internal structure that displays a varying degree of organization within the different parts of the cartilage. This degree of organization within the cartilage changes predictably along the depth of the tissue, making it at the same time interesting but challenging candidate for qMRI studies. The organized nature of articular cartilage is the result of the organisation of collagen fibers within the tissue. Close to the surface of the cartilage the average direction of these fibers is oriented parallel to the surface, but turns perpendicular to the surface in the deeper layers of the cartilage.

Early qMRI studies of anisotropic tissues observed that the T_2 is dependent on the orientation of the tissue in relation to the main magnetic field. This effect, seen both in research and clinical measurements, is often referred to as the magic angle effect [2, 4, 5, 6]. The angular dependence of T_1 and T_2 relaxation processes is a subject with a long history of studies with multiple published articles [1, 5, 7, 8, 9, 10, 11]. In many of these studies the tissue sample has been measured only a handful of times, resulting in the collected measurement data often only accounting for a small set of possible sample orientations. This in turn has lead to these descriptions of angular dependency to be potentially incomplete. In addition, the cartilage samples used in these studies have most often been small osteochondral plugs, with only a small sample of cartilage compared to a full joint. The aim of this paper is to study the angular dependence of the T_2-relaxation in bovine articular cartilage using a large sampling of sample orientations, and creating a measurement set up closer to that found in a clinical environment. The measurements were performed on bovine articular joint samples using a 3 T clinical MRI device. An additional goal of the study was to design and manufacture a device enabling the accurate reorientation of a full-size bovine stifle joint within the bore of a clinical MRI device.

2 Articular cartilage

Articular cartilage (AC) is a connective tissue located at the end of the bone surfaces of many articulating joints. Its primary functions during joint locomotion are to provide a near frictionless surface in joints and to process the forces applied to bone ends [3, 12]. Unlike many tissues surrounding AC, it itself is both avascular and aneural. This lack of vasculature in AC means that both delivery of nutrients and removal of waste happen solely via passive diffusion. The lack of active nutrient intake slows down the tissue's capacity for self-repair which, when combined with the lack of pain reception in the cartilage, means that damage to the AC is often both painless and slow to repair. The primary components of AC are water, collagen, proteoglycans and chondrocytes [13, 14]. Chondrocytes are the only living cell phenotype in cartilage. While they occupy only approximately 2% of the total volume of human cartilage, they are solely responsible for synthesizing and maintaining the cartilage over its lifetime. The concentration and properties of chondrocytes change across different cartilage layers [3, 13, 15].

The structure of AC can be described using two phases: a solid and a liquid phase [3]. The solid phase consists mainly of collagen and proteoglycans (PG). The liquid phase fills the rest of AC volume and consists mainly of water and water soluble ions and nutrients. The majority of the AC volume is filled by a semi-solid extracellular matrix (ECM), formed of a network of collagen and PG molecules. The liquid phase fills the voids of the solid matrix, giving AC its structure. The major components of the ECM in adult human cartilage are collagen, consisting primarily of type II and additionally XI collagen (15-20% of the wet weight (w.w.) of cartilage), proteoglycans (3-10% w.w.) and water (65-75% w.w.) [13, 16]. The space around chondrocyte cells differs from the wider ECM in both composition and function and is referred to as the pericellular matrix (PCM). The PCM forms clearly defined structural units called chondrons around the cells. While crucial to the metabolism of the wider AC, the PCM itself amounts to only a small portion of the total volume of the liquid phase. The PCM consists of water, PG, collagen of types VI and IX and other non-collagenous proteins and nutrients [3, 15].

Collagen is a structural protein and a major structural component of AC, consisting of approximately 1/2 to 2/3 of the dry weight of adult human cartilage. The main building block of collagen is the tropocollagen molecule, which consists of three amino acid chains. Each of these chains consists of repeating segments of glycine-proline-Y or glycine-X-hydoxyproline, where X and Y can be any amino acid. A tropocollagen molecule is assembled in a so called "coiled-coil" structure. Each of the three amino acid chains are wound

in a left-handed coil, and these three twisted coils are then wound in a right-handed triple helix. The resultant tropocollagen molecule resembles a rod approximately 300 nm in length and 1.5 nm in diameter [3]. The collagen in the ECM consists of type II and XI collagen, while the collagen in the PCM consists of types VI and IX. Collagen of type II is the primary type of collagen found in adult human cartilage. Collagen II is a fibrillar protein, where the coiled-coil tropocollagen molecules are assembled into long fibrils of 50-80 nm in length via covalent crosslinking and non-covalent interactions between the individual coils. The linked collagen fibrils form a vast crosslinked network that functions as a scaffold for the ECM and other proteins.

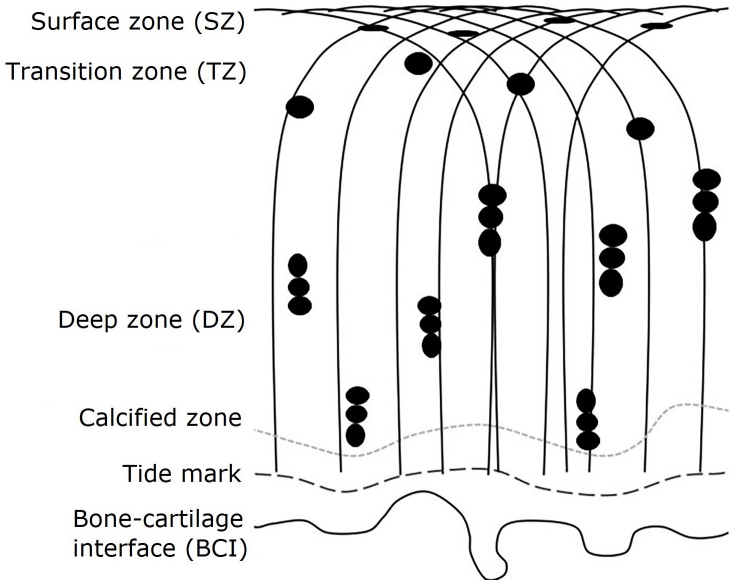

Figure 1: Schematic representation of average collagen fiber direction according to the Benninghoff arcade model [17]. In this model the average lines of fibrillar direction in cartilage begin with an overall tangential alignment in the surface zone and gradually 'arcade' into a perpendicular alignment to the surface in the deep cartilage before attachment to the subchondral bone at the bone-cartilage interface [18].

Proteoglycans are large macromolecules that contain a protein core and covalently attached sulfated glycosaminoclygan (GAG) molecules. The protein core has a molecular weight of $\approx$ 25000 Da and can have more than 100 GAG molecules laterally bound to the main protein in a branched, bottlebrush-like structure [7]. Due to their very large molecular weight, proteoglycan molecules have low mobility in cartilage. They are most often packed to a small fraction of their fully extended volume and are entrapped

between the collagen fibrils. The negatively charged GAGs are the primary source of the fixed electric charge in the ECM. The intermolecular electrostatic repulsive force between the GAG groups contributes to the stiffness and elasticity of the cartilage tissue. Proteoglycans are also a major component of cartilage hydration. The negatively charged GAGs attract free-floating Na^+ ions that in turn bind large amounts of water, acting like macromolecular "sponges" that osmotically retain water in cartilage tissue [3, 7, 16].

AC composition has notable variation throughout its depth, and can be separated into four different histologic layers (Figure 1). These zones are characterized by their differences in both the organisation and distribution of PG and collagen. They are called, in order from surface to subchondral bone, the surface, transition, deep, and calcified zone [3, 12, 15].

The first layer on the surface of the cartilage is called the superficial zone (SZ). It plays a major role in the cellular metabolism and mechanical properties of the cartilage. In this zone the collagen fibers are aligned parallel to the cartilage surface giving the structure a high resistance to shearing forces [15]. The thickness of SZ varies depending on the location of the cartilage, ranging from 3-20% of total cartilage thickness. The surface layer contains a high concentration of collagen fibers, but a low number of chondrocytes [3, 19, 13].

The transitional zone (TZ) is located directly below the SZ of cartilage. Sometimes also referred to as the middle zone, the TZ is where the cartilage composition and collagen fiber orientation gradually transition from SZ to that of the deeper zones. Close to the surface of the TZ, the collagen fibers are initially oriented almost parallel to the surface, but gradually change to perpendicular to the surface as the distance from the surface increases. The number of chondrocytes in TZ is also the lowest near the SZ and increases in the deeper TZ. Since the defining properties of the TZ experience continuously change along its depth, declaring any exact boundaries between TZ and its neighbouring zones is a difficult undertaking. Depending on the location of the cartilage in a joint the thickness of TZ can vary significantly, ranging from 15% to up to 60% of total cartilage thickness [3, 8, 13].

The deep zone (DZ), sometimes referred to as the radial zone (RZ), is located directly below the TZ. In DZ, the collagen fibrils are structured in bundles oriented perpendicular to the surface. The ECM of the DZ contains the most proteoglycans and the least fluids compared to the other cartilage zones. Compared to the regions above it, the structure of the DZ is also considered most uniform and highly organized [3, 8, 13].

The calcified zone is located beneath the radial zone, and is responsible for fixing the cartilage to the underlying bone. This zone contains partially calcified and mineralized cartilage tissue cemented in the subchondral bone. [3]

The orientation of these anchoring fibrils is perpendicular to the subchondral bone, extending from it to the articular surface. These fiber structures are called Benninghoff's arcades [17]. Histological staining of the cartilage often displays a wavy line denoting the mineralisation front of the calcified cartilage. This tidemark is used as the distinctive line between the radial zone and the calcified zone [3].

3 Magnetic resonance imaging

Magnetic resonance imaging (MRI) is a popular imaging modality both in medical and research fields. Originally discovered in the 1940s and first used in a clinical setting in the 1980s [3], MRI utilizes the phenomenon known as nuclear magnetic resonance (NMR) to noninvasively measure the spatial distribution of specific atomic nuclei or electrons within the imaging target [3, 20]. This is accomplished by using the principles of nuclear magnetic resonance to measure the precession of nuclear spins in a magnetic field. When exposed to a strong magnetic field the magnetically susceptible spins begin to precess around the field. This precession along the field causes an equilibrium state to form between spin orientations, leading to a net magnetisation within the sample. This equilibrium state can then be disturbed using a radio frequency (RF) pulse. As the disturbed spins recover to their original orientation, the change in precession causes the spins to emit an electromagnetic wave, which can then be measured via the current it induces into nearby detection coils. This time-domain signal can them be converted into frequency domain. MRI is well suited for clinical imaging of soft tissues due to its noninvasive nature, lack of ionizing radiation, good soft tissue contrast and easy scalability from single organ to full-body imaging [3, 20, 21].

3.1 Nuclear magnetic resonance

All visible matter is formed of molecules, which in turn are made of atoms. Atoms consist of a positively charged nucleus, made out of electrically neutral neutrons and positively charged protons, which is orbited by a cloud of negatively charged electrons. Both protons and neutrons consist of a combination of three up- and down-quarks. A proton consists of two up- and one down-quarks (uud), while a neutron consists of one up- and two down-quarks (udd). In the Standard Model of particle physics all elementary particles with mass, such as electrons and quarks, are called fermions [22]. All elementary particles exhibit an electromagnetic property called spin. While being somewhat analogous with angular momentum present in classical mechanics; spin

is a quantum mechanical phenomenon, and as such it can only have discrete values of $\frac{n}{2}$, where $n \in \mathbb{R}$. The spin of quarks and other fermions is $\pm\ 1/2$. In their ground states the spin of a protons is $1/2$ and the spin of a neutron is $-1/2$. This is due to the quarks of opposing spins within both particles cancelling each other out. Atomic nuclei are similarly formed of protons and neutrons with opposing spins. If the nucleus is formed of an even number of protons and neutrons the opposing spins once again cancel each other out, resulting in a spin of 0 in its ground state. Otherwise a resultant spin of $\pm 1/2$ will remain in the nucleus. These kinds of particles are referred to as magnetic nuclei; f.ex. a hydrogen nucleus consisting of a single proton is magnetic and has a spin of $\pm\ 1/2$ [22].

When, for example, a sample containing water is placed in an external magnetic field, the spins of the water ^{1}H nuclei will begin to precess around the direction of the magnetic field. While nuclear spin is a quantum mechanical phenomenon, spin precession can be viewed as analogous to the rotation of a classical spinning top. The frequency of this precession ω is called Larmor frequency and it can be described using the following equation:

$$\omega = \gamma B, \tag{3.1}$$

where γ is the gyromagnetic ratio of the precessing particle and B is the strength of the local magnetic field experienced by the particle. For example a proton has a gyromagnetic ratio of $2.675 \cdot 10^8$ rad/s/T. When placed in a magnetic field of 3 T this corresponds to a Larmor frequency of $\omega = 802.6 \cdot 10^6$ rad/s $= 127.7$ MHz. The spin precession at the Larmor frequency is called Larmor precession.

As the precessing spins interact with the constantly fluctuating magnetic fields caused by their surrounding magnetic nuclei, both the magnitude and direction of the local magnetic field experienced by an individual spin changes over time. This results in the precession angle of an individual spin to slowly 'wander' across the full range of possible cone angles, which by itself would cause the angle distribution to be fully isotropic. This is however not the case, as the finite temperature of the system causes the orientations aligned along the direction of the magnetic field to have slightly lower magnetic energy, resulting in the probability of a precession cone of a spin being very slightly biased towards the direction external magnetic field. The constantly changing angle of the spins' precession cone combined with the small direction bias caused by the external magnetic field results in a slightly larger population of spins to be aligned along the direction of the magnetic field at any given time, forming a thermal equilibrium. This thermal equilibrium results in the sample acquiring a small net magnetic moment along the field [3, 23]. This

moment, called the net magnetisation $\mathbf{M}_0$ depends on the strength of the magnetic field $\mathbf{B}_0$, the gyromagnetic ratios γ of the nuclei in the sample, the temperature T of the sample, and the density ρ of the magnetic nuclei in the material. It can be described using the equation

$$\mathbf{M}_0 = \frac{\gamma^2 \hbar^2}{4kT} \rho \mathbf{B}_0, \tag{3.2}$$

where $\hbar$ is the reduced Planck constant $\hbar = h/2\pi$ and k is the Boltzmann constant [3]. The direction of the net magnetisation is often referred to as the polarisation axis. The existence and manipulation of this net magnetisation within small volume units of matter is the basis of magnetic resonance imaging [3, 20].

3.2 Nuclear magnetic relaxation

The spin equilibrium state formed by the external magnetic field B_0 can be destabilized by using an electromagnetic pulse. The frequency band of this pulse can be chosen to affect only certain magnetic nuclei within the sample. In medical MRI the proton (or ^{1}H) is the most commonly studied particle. The frequency band of this pulse during proton MRI is generally in the radio-frequency range, lending the pulse its name: the RF-pulse. This study also focuses on the nuclear magnetic relaxation of the proton, allowing the naming convention to be used without issue. The RF-pulse can be used to reorient the polarisation axis of the precessing spins in a process called spin excitation. As the direction of net magnetisation in equilibrium follows the polarisation axis, spin excitation also causes the direction of the net magnetisation to be reoriented along this new polarisation axis. Stopping the RF pulse conversely ends the spin excitation, resulting in the net magnetisation returning to its original equilibrium direction and magnitude through a process called nuclear magnetic relaxation. This relaxation can be split into two components: longitudinal and transverse relaxation, each with their own time scales and relaxation mechanisms [20].

During most spin excitation experiments the RF-pulse is used to align the net magnetisation of the precessing spins to be perpendicular to the original polarisation axis. This effectively causes the longitudinal magnetisation along the original z-axis to disappear as long as the RF-pulse is active. As the RF-pulse ends, the slight bias in spin magnetic moment direction caused by the pulse also disappears. This causes the net magnetisation to return back to its thermal equilibrium value and direction, resulting in the longitudinal magnetisation also returning to its equilibrium value $M_0\hat{z}$ [23]. The regrowth of longitudinal magnetisation M_z after spin excitation is generally referred

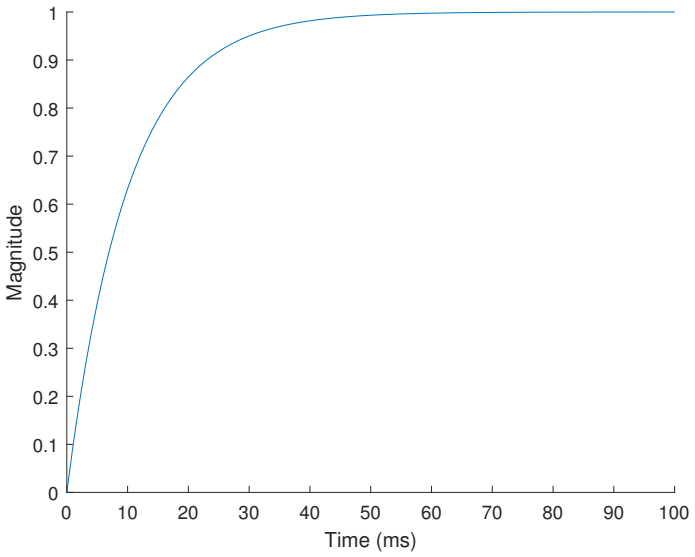

Figure 2: Equation 3.3 plotted as an example of the exponential regrowth of longitudinal magnetisation. The constants have been given following values: $M_0 = 1$, $K = 1$ and $T_1 = 10$ ms

to as longitudinal or T_1 relaxation, and it behaves in a manner similar to an exponential regrowth equation [3, 20].

An empirically determined relaxation time constant T_1 for the spin-lattice interactions can be used to create a model for the change in parallel magnetisation after spin excitation.

$$M_z = M_0(1 - Ke^{-t/T_1}), \tag{3.3}$$

where K describes the coefficients affecting the regrowth rate of M_z and depends on the type of experiment being performed.

Directly after spin excitation the RF-pulse has aligned the net magnetisation to be perpendicular to the polarisation axis, resulting in the transverse magnetisation $M_{x,y}$. Once the RF pulse ends, the precessing spins begin to lose their quantum coherence, leading to the transverse magnetisation rapidly decaying. This irreversible loss of transverse magnetisation is referred to as transverse or T_2 relaxation. Similarly to parallel magnetisation, an experimental transverse relaxation time constant T_2 can be determined for $M_{x,y}$ using the following equation:

$$M_{x,y} = M_0 e^{-t/T_2}, \tag{3.4}$$

where M_0 is the net magnetisation from equation 3.2.

As the RF-pulse reorients the polarisation axis, it also aligns the phases of the precessing spins. Once spin excitation ends the precessing spin vectors begin to interact with the small inhomogeneities of the magnetic field, causing small position dependent phase differences within the spin system. As time goes on these small spatially dependent phase differences grow in magnitude and eventually lead to the spin system completely dephasing. This leads to an additional exponential decay of the transverse magnetisation as the opposing magnetisation vectors within the dephasing spin system cancel each other out [3, 20, 23].

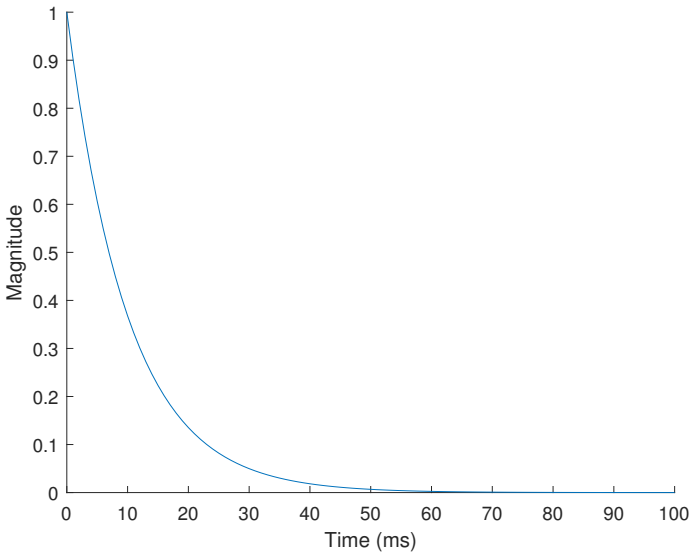

Figure 3: Equation 3.4 plotted as an example of the exponential decay of transverse magnetisation. The constants have been given following values: $M_0 = 1$, $K = 1$ and $T_1 = 5\ ms$

Combining the effects of transverse relaxation and dephasing gives a so-called apparent transverse relaxation time T_2^*, which can be show as:

$$\frac{1}{T_2^*} = \frac{1}{T_2} + \frac{1}{T_2'}, \tag{3.5}$$

where T_2' is the relaxation time constant resulting from the dephasing spin system. In a fully uniform B_0 field $T_2 = T_2^*$, but any field inhomogeneities

will invariably cause $T_2^* < T_2$ as is the case in almost all real-world systems. Unlike spin relaxation, the dephasing caused by the inhomogeneities of the magnetic field is a fully reversible process [3, 20].

3.3 Magnetic resonance imaging

Magnetic Resonance Imaging (MRI) takes advantage of the magnetic properties of precessing spins to generate images of the spatial mapping of the studied nuclei within the imaging subject. As explained in section 3.2, spin excitation is accomplished using a transient Larmor-frequency RF-pulse. This pulse creates a new oscillating magnetic field B_1, which changes the direction of the polarization axis. The angle between the new rotated polarisation axis and the main magnetic field is called a flip angle θ_f and can be described using the following equation:

$$\theta_f = \gamma B_1 \tau, \tag{3.6}$$

where γ is the gyromagnetic ratio of the precessing spins, B_1 is the strength of the perpendicular magnetic field and τ is the length of the RF-pulse. The most commonly used flip angles are 90° for perpendicular spin excitation and 180° for spin-echo measurements. Similarly to the shimming fields, the RF-pulses are created using separate RF-coils in close proximity to the imaging subject [3, 20].

The B_0 fields used to create the prerequisite spin equilibrium in the imaging sample are generally in the range of $1.5 - 3$ T in clinical MRI devices, but can go up to and beyond 9 T for research purposes. For comparison, the magnitude of the Earth's magnetic field at the planet's surface ranges from 25 to 65 μT [24]. To create and maintain a magnetic field of this magnitude, superconducting electromagnets are used in most mid- to high-field MRI devices. The electromagnets achieve superconductivity by being cooled to only a few degrees Kelvin, commonly accomplished via the use of liquid helium and nitrogen. As the magnets are superconducting, they require no additional current to maintain the B_0 field once it is created. This causes the strong magnetic field to be always active, a fact that requires specific precautions to be taken when operating at or around any functioning MRI device. Placing an object or a patient in an MRI device invariably causes distortions in the main magnetic field. These inhomogeneities are most often corrected via the use of additional electromagnets called shimming coils [3]. Even in such a strong magnetic field, the magnetisation of a single ^{1}H spin is still too weak to be individually detected. Instead, MRI techniques divide the sample into small volume units (voxels) and measure the net magnetisations

within each individual voxel. Since the magnetisation within each voxel is dependent on its proton density (equation 3.2), the signals from neighbouring voxels can be used to map proton distribution across the sample.

As the net magnetisation across the sample returns to its equilibrium value after spin excitation, the precessing spins emit electromagnetic waves. These waves are detected using measurement coils, that measure the electric current induced in them by the emitted radiation. The measurement coils are in general placed as close to the imaging subject as possible in order to acquire the strongest possible signal. The frequency data obtained from the measurement coils is collected in a format known as k-space, which maps the collected frequencies to phase differences in the form of a 2D or 3D matrix. An MRI measurement with a single frequency and phase difference collects data from the entire sample, which corresponds to a single pixel in the k-space. In more commonly used single-line measurements a single measurement collects data from a single phase difference and multiple different frequencies, corresponding to a horizontal line in k-space. This phase and frequency data of the k-space can be transformed into an image in image-space (or "real-space") using an inverse Fourier transform [3].

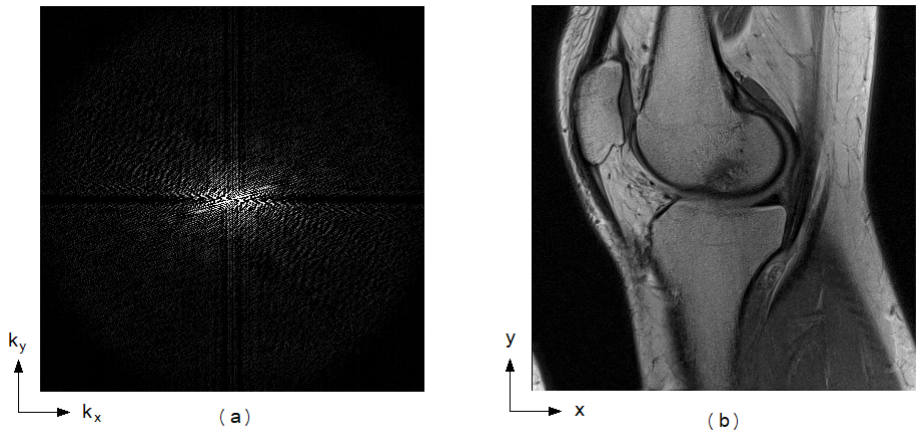

Figure 4: (a) Raw frequency and phase data of a human knee in a k-space array and (b) corresponding image data calculated using inverse Fourier transformation.

The creation of a k-space signal requires the use of many additional magnetic fields called gradient fields or gradients. These gradient fields code the required phase and frequency differences in the precessing spins before and during measurement.

The Larmor frequencies of spins are dependent on their surrounding magnetic field as shown in Eq. (3.1). An RF-pulse causes a full spin excitation

only if the Larmor frequency of the precessing spins is the same as the frequency of the pulse. By altering of the strength of magnetic field linearly along the length of the imaging subject, a spatially dependent Larmor frequency gradient can be created within the sample. This causes a spin excitation pulse of a discrete frequency band to be in resonance with only the spins contained within a small slice perpendicular to the gradient field. This process of selective spin excitation is called slice selection. For example, if the slice selection gradient is placed along the z-axis the selected slice will be on the x, y-plane. Changing the midpoint and width of the frequency band of the RF-pulse, the width of the selected slice can also be changed. The slice selection is generally accomplished by using a separate gradient field G, which is typically generated using a minimum of three separate coils aligned in x-,y- and z-directions, where z is the direction of the main magnetic field. This gradient is also often referred to as the slice selection gradient G_S. The combined magnetic field and gradient field in the z-direction can be described using the following equation:

$$\vec{B} = B_0 + (G_x x + G_y y + G_z z)z, \tag{3.7}$$

where $G_{(x,y,z)}$ are the three directional components of the gradient field.

In its simplest form, a single MR measurement correlates to a line in k-space, containing a spread of frequencies at a single phase difference. This single phase difference is created after spin excitation using the phase encoding gradient G_P aligned orthogonally to the direction of the slice selection gradient. When active, the slice selection gradient causes a phase difference in the precessing spins of the selected slice. The phase encoding gradient also corrects this phase difference during phase encoding. The frequency differences during measurement are created using a readout gradient G_{RO}, sometimes referred to as frequency encoding gradient G_f. This gradient, aligned along the G_S gradient and orthogonally to the G_P, is used to create a frequency difference between the precessing spins within the slice. The readout gradient is active during signal acquisition, meaning that a single measurement contains information from a single phase difference and multiple different frequencies corresponding to a single line in k-space. While the single-line method is a commonly used technique, the process of measuring each individual line in k-space is comparatively slow. Measurements with fast imaging and echo times can employ a wide variety alternate k-space trajectories, both in Cartesian and non-Cartesian coorinates, each with their own benefits and drawbacks. Commonly used trajectories include f.ex. radial and spiral trajectories [25, 26].

The successful acquisition of an MRI image depends on the correct application of the gradient fields in a carefully orchestrated sequence of elec-

tromagnetic pulses, aptly referred to as a *pulse sequence*. One commonly used pulse sequence is the spin-echo sequence and describing it gives a good overview on the basic function of the MRI. The spin-echo sequence is used in the measurement of transverse magnetic relaxation, and is accomplished using a series of 180° spin excitations. Immediately after the excitation pulse the transverse magnetisation is at its strongest value, as all of the precessing spins are at the same phase. Afterwards the spin-spin interactions cause the precessing spins to rapidly dephase as the emerging opposing magnetisation components cancel each other out. If left undisturbed this dephasing will inevitably lead to the decay of the transverse magnetisation back to its equilibrium value along an exponential decay curve. By applying a 180-degree inversion pulse during this dephasing, its direction can be reversed. This causes the transverse magnetisation to refocus after a certain time, creating a measurable 'echo' of the original transverse magnetisation. The time between spin excitation and signal measurement is called echo time (TE). If the spin-echo measurement is repeated, the time between each transverse spin excitation is called repetition time (TR). The 180° refocusing pulse can be repeated multiple times and a signal can be measured after each subsequent TE. This series of echoes, sometimes referred to as a echo train can technically be repeated for as long as a measurable amount of transverse magnetisation exists within the sample. This pulse sequence is called a multi echo spin-echo (MESE) sequence. The strength of the refocused magnetisation and the resulting signal is weaker after every subsequent echo due to the irreversible T_2 relaxation effects.

The signal-to-noise ratio (SNR) in MRI depends largely on the size of the voxels used and the strength of the main magnetic field B_0. Reducing the size of the voxel also reduces the SNR, as the net magnetisation within a voxel is dependent on the amount of protons within within the voxel. The strength of the B_0 field affects the strength of the net magnetisation within a voxel as seen in Eq. (3.2). A common way of increasing the SNR of a measurement is to repeat the same measurement sequence multiple times and calculate the averaged signal for each k-space pixel. During signal collection the current signal is amplified and is converted from analogue to a digital signal using an analogue-to-digital converter.

Contrast between different tissues in MRI is the result of their differing T_1 and T_2 relaxation times and proton densities. This contrast can be further emphasized by altering the pulse sequence to be more sensitive to the signal from either transverse or longitudinal relaxation effects. This process is commonly referred to as signal weighting. The signal intensity of an MRI measurement depends on the following equation:

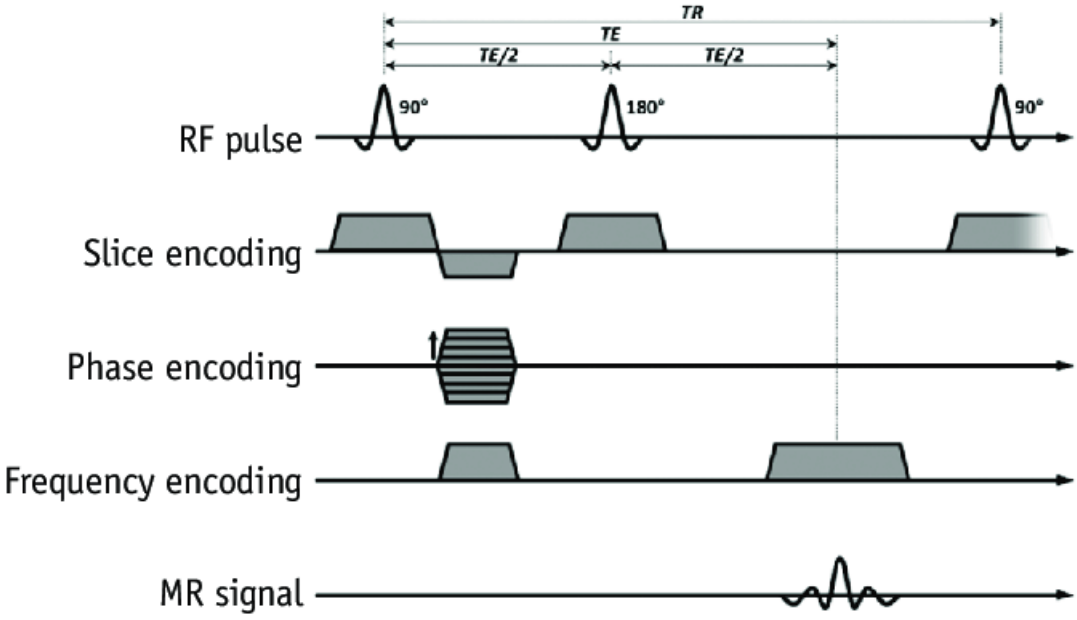

Figure 5: A schematic representation of a simple single-echo spin-echo MR sequence [27].

$$S = \rho \left(1 - e^{\frac{\mathrm{TR}}{T_1}}\right) e^{\frac{-\mathrm{TE}}{T_2}}. \tag{3.8}$$

For example a pulse sequence emphasizing T_2 can be created by selecting a TR that is notably larger than the T_1 of the tissue, and a TE that has roughly the same value as T_2. This causes the longitudinal magnetisation to fully relax between spin excitations, making T_2 the dominant contributor to the changes in signal intensity during measurement.

These relaxation weighted MRI images can then be used to generate maps depicting the corresponding relaxation time constants within parts of the imaging subject, using a process called relaxation mapping. By first collecting a set of images using different echo and repetition times, a mathematical model depicting the relevant relaxation type can be fitted onto the dataset of each voxel. The relaxation times can then be extracted from each fit and mapped as a value for the corresponding voxel, creating a map of relaxation times within the target slice. In the case of T_2 mapping for example, the sample is imaged multiple times at different echo times using a T_2 weighted imaging sequence. A relaxation equation similar to Equation (3.4) is then individually fitted to the echo-time sets of each voxel, and the T_2 values collected from them are set as the voxel values in the resultant map. These

types of maps are called T_1 and T_2 maps depending on the type of relaxation studied.

4 Transverse relaxation in articular cartilage

As shown in Section 2, articular cartilage contains a large quantity of collagen fibers at various levels of structural organisation across the depth of the cartilage. The high structural organisation of the solid materials within AC leads to a high degree of structural anisotropy. The orientation dependency of MR relaxation times arising from this anisotropy makes the MRI of AC challenging, especially in a clinical setting. This combined with the depth-dependent structure organisation and macromolecular composition makes articular cartilage both challenging and interesting subject for MRI studies [3, 28]. Understanding the mechanisms behind ^{1}H orientation anisotropy in AC would allow its effects to be mitigated or potentially exploited in clinical MRI.

The history of the MR orientation dependency in biological tissues dates back to the 1960s. Early T_2-weighted NMR measurements in solid materials would see substantial changes in relaxation times when the sample was reoriented between measurements [3]. As solid materials exhibit reduced molecular mobility compared to soft tissues, they generally have shorter transverse relaxation times and resultantly smaller signal intensities during T_2 weighted imaging. These studies would use the orientation anisotropy of the sample to increase the signal intensity and improve the SNR of the imaging by turning the sample in relation to the B_0 field to increase the transverse relaxation time [3, 4, 29]. For soft tissues the orientation anisotropy was first discovered in a study in 1962 by Berendsen et al. [30] In this study NMR was used to measure the hydration properties of tendon samples, resulting in the discovery of a strong angular dependence in proton signal intensity depending on the sample orientation [30]. This phenomenon, while commonly used in solid-state NMR, did not immediately see any further research in biological tissues until 1985, when it was rediscovered by Fullerton et al. [31] during their study on the NMR relaxation properties of tendons. In their study the T_2 weighted signal from a human in vitro tendon sample would reach peak intensities when the sample was rotated in such a way that the tendon fiber orientation was at angles $\theta \approx 55°$ and $\theta \approx 125°$ with respect to the main magnetic field [31].

The difference in observed ^{1}H relaxation times within articular cartilage is fundamentally the result of the hydrogen nuclei interacting with the magnetic fields produced by the surrounding atoms and molecules [3, 23]. In

all water containing tissues, the hydrogen nuclei of a single water molecule interact with each other and with the nuclei of neighbouring water molecules via electromagnetic interaction. This interaction causes a nucleus to "feel" the electromagnetic fields generated by their neighbouring charged particles. The freedom of movement a water molecule has within the tissue directly affects both the amount of particles its hydrogen nuclei can interact with, and the frequency of these interactions [23]. The dipole-dipole interaction of two hydrogen nuclei can be modeled as two interacting current loops. In a strong magnetic field these dipoles precess around the main magnetic field. Assuming the spins are parallel to the z-axis, the interaction between two dipoles depends on the z-components of their respective magnetic fields. For dipole 1 this z-component B_z depends on its radial component of B_r and on its tangential component B_θ at dipole 2 [4]. It can be written as

$$B_z = B_r \cos\theta - B_\theta \sin\theta, \tag{4.9}$$

where θ is the angle between the dipoles in relation to the z-axis. B_r and B_θ depend on the distance between the dipoles r and on their magnetic dipole moment m.

$$\begin{cases} B_r = \frac{2m}{r^3} \cos\theta \\ B_\theta = \frac{m}{r^3} \sin\theta \end{cases} \tag{4.10}$$

By using equations 4.9, 4.10 and the identity $\sin^2\theta = 1 - \cos^2\theta$, the B_z component can be shown to be

$$B_z = \frac{m}{r^3}(3\cos^2\theta - 1). \tag{4.11}$$

Equation 4.11 shows that the intramolecular dipole-dipole interaction disappears when $3\cos^2\theta - 1 = 0$, which corresponds to $\theta \approx 55°$. This effect has been confirmed by multiple studies on the orientation of ordered structures within biological tissues strongly affects the intensity of T_2- weighted imaging [1, 3, 4, 32, 33]. In these studies the changes in T_2 weighted signal intensities have been seen to reach their peak values around angles where the residual dipole-dipole interaction reaches its minimum in accordance with equation (4.11), or in other words when the condition

$$3\cos^2\theta - 1 = 0 \tag{4.12}$$

is fulfilled. This phenomenon is known in clinical settings as the magic angle artefact or more generally as the magic angle effect [3, 4, 21].

The T_2 relaxation time of a sample of articular cartilage depends mainly on three factors: the degree of organisation of the collagen fibers, the chemical properties and the molecule distribution of the ECM, and the amount of water in the tissue [3]. In AC, the structure of the collagen fiber network limits the free movement of the water molecules within the tissue. The more constrained surroundings also limit the movement of the water molecule's covalently bound hydrogen atoms in relation to each other [3]. If the orientation of the collagen fibers is sufficiently organized in a certain direction, this limiting factor gives rise to the anisotropy of the transverse relaxation [5, 6, 29]. When a cartilage sample is oriented to one of these magic angles during MRI, the frequency of dipole-dipole interactions between neighbouring protons are minimized. As these interactions are the primary contributor to the shortening of T_2 within cartilage, reducing their frequency results in longer T_2 and a stronger T_2-weighted signal [3]. During MRI of articular cartilage this effect can be seen as large changes in intensity of the T_2-weighted images as a function of the sample orientation with respect to the main magnetic field B_0. The water content of AC is restricted by the proteoglycan molecules within the ECM. The negative fixed charge distribution of the GAGs in PG prevents new water from entering the cartilage, and at the same time restricts the mobility of the water molecules bound to the GAGs [34]. Applying a mechanical load to the cartilage before measurement causes water to leave the cartilage, which has been shown to lead to shorter T_2 times [35].

The magnetic fields experienced by hydrogen nuclei in cartilage during MRI depend both on the external magnetic field B_0 and on the small magnetic fields caused by their molecular surroundings. As these surroundings are constant motion and interaction with each other, the nuclei can experience a local time-dependent magnetic field of varying strengths and directions during normal MR imaging times. In solid materials, such as bone or teeth, hydrogen nuclei are bound via strong proton-proton couplings, resulting in an ultrashort T_2^* and a rapid net magnetisation dephasing before normal MR signal detection times, making these materials largely invisible to MRI. Free water molecules, such as those present in water and fat, rapidly create and break these hydrogen bonds with a time constant of roughly 200 fs, during which protons rapidly exchange between neighbouring water molecules [3]. This, coupled with rapid molecular diffusion in mobile liquids, results in any given hydrogen nucleus sampling a large number of atomic environments during normal water MRI relaxation times. These rapidly varying magnetic fields experienced by the hydrogen nuclei result in this rapid phase shift of a single nucleus averaging to zero, thus preventing ultrafast dephasing and allowing T_2 within cartilage to be detected during standard MRI imaging times [3].

While there is clear scientific consensus on the existence of the magic angle effect, there are varying theories to the exact mechanisms behind the observed angle dependence [3]. In collagenous tissue, the molecular motion of protons has been theorized to be affected by the formation of water bridges between the water molecules and the collagen fibers [3]. The hydrogen atoms of water molecules close to binding sites in the collagen backbone can form either single or double water bridges, directly limiting the intramolecualr motion of the hydrogen nuclei bound to the water molecule [3]. These water bridges limit the intramolecular motion of the bound water, further shortening the T_2. The orientation dependency of the T_2 relaxation is caused by the organization of the collagen fiber structure. The interaction between water molecules and proteoglycans has also been shown to depend on the orientation of the tissue [36].

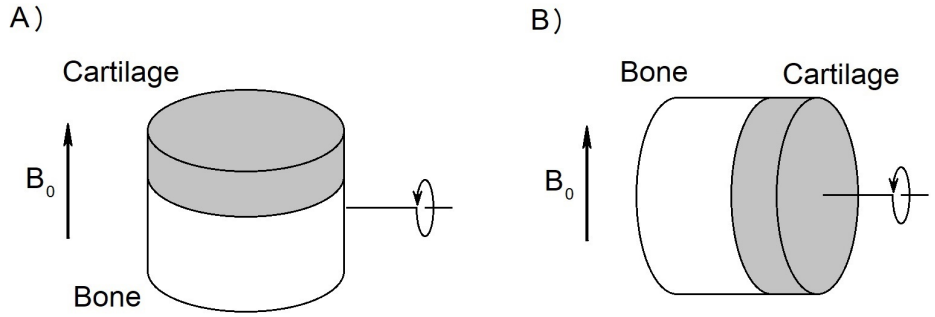

Figure 6: Example figures depicting two rotation schemes for an ostheocondral plug taken from a joint sample. A) Rotation along an axis perpendicular to the cartilage surface normal. B) Rotation along an axis parallel to the cartilage surface normal.

Many mathematical models exist for describing the orientation dependence observed in anisotropic biological tissues [3]. Often these divide the studied relaxation into an anisotropic component and an orientation-independent isotropic component. In these models the angular dependence of the anisotropic model appears to follow the square of equation (4.12) [3]. The relaxation rates of both the isotropic and anisotropic components can be combined additively to show the total relaxation rate of the sample [3, 6]. This can be presented as the following equation:

$$\frac{1}{T_2} = R_2 = R_{2,i} + R_{2,a}(3\cos^2\theta - 1)^2/4, \tag{4.13}$$

where $R_{2,i}$ is the isotropic component, $R_{2,a}$ is anisotropic component. In articular cartilage the angle θ describes the angle between the collagen fiber orientation and the magnetic field B_0.

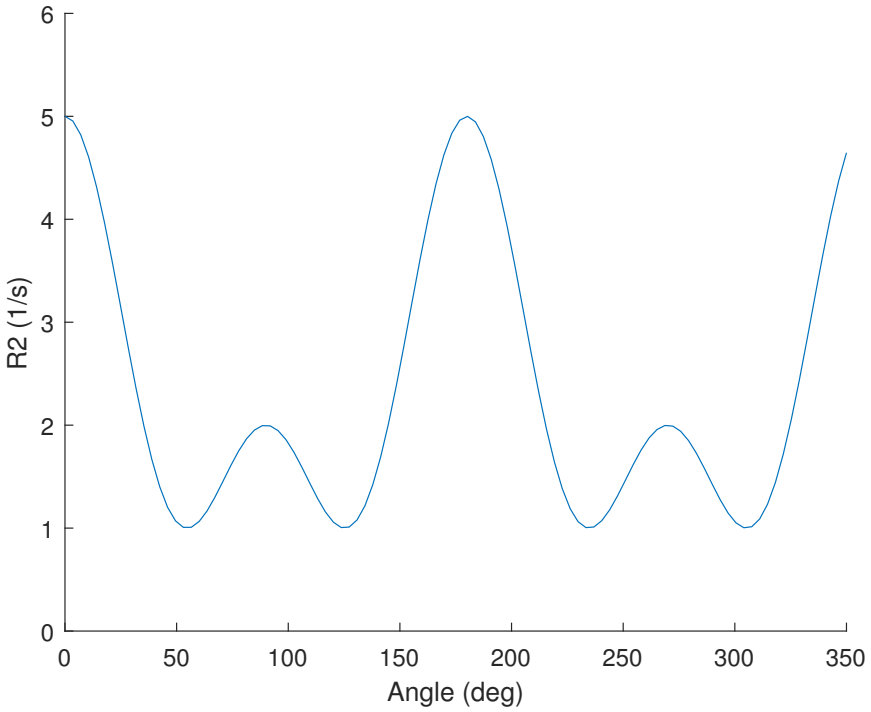

Figure 7: An example plot of the anisotropy model for transverse relaxation rate R_2 as shown in equation (4.13). The constants used in the plot are $\mathrm{R}_{2,\mathrm{i}} = 1\ \frac{1}{s}$ and $\mathrm{R}_{2,\mathrm{a}} = 4\ \frac{1}{s}$.

As the properties of articular cartilage change along its depth, so too does anisotropic behaviour of T_2 relaxation. Since articular cartilage can be split into multiple sections based on their differing properties (Section 2), so too can the transverse relaxation in AC be separated into three distinct zones: surface, transitional and deep zone [28, 32, 37].

Unlike in the deeper layers of the cartilage, in the surface zone the collagen fibers are oriented parallel to the cartilage surface [19]. The spread of fiber orientations along the surface is generally assumed to be isotropic. This results in the cartilage displaying little orientation anisotropy when the sample is rotated. When rotated along the normal of the cartilage surface (Figure 6 B), the SZ has in cases displayed notably strong T_2 anisotropy, suggesting that the surface fiber orientation might not be as isotropic as previously suggested [38].

In the transitional zone of cartilage the majority of the collagen fibers close to the cartilage surface are oriented parallel to the surface, while in the deeper part of the TZ fiber distribution is more perpendicular to the surface.

This gradual change in fiber orientation leads to an increase in orientation anisotropy in the sections of TZ furthest from the cartilage surface [10]. This growing fiber organisation results in the lower sections of TZ also displaying a degree T_2 anisotropy, albeit still to a lesser degree than that of the deeper cartilage zones [3].

In the deep zone of cartilage the collagen fibrils are packed tightly in bundles, which in turn are aligned perpendicularly to the subchondral bone with a high degree of organisation. This results in a strong T_2 anisotropy during rotation along axes perpendicular to the cartilage surface normal (Figure 6 A), and a largely isotropic transverse relaxation along rotation along the cartilage surface normal (Figure 6 B) [38]. In the deeper parts of the DZ closer to the bone-cartilage interface, the T_2 anisotropy becomes increasingly weaker and eventually disappears in the calcified cartilage zone [10].

5 Materials and Methods

5.1 Rotation platform

In order to study the anisotropy of the cartilage surfaces of the bovine stifle joint sample, a way to accurately change the sample orientation between measurements was needed. The design of the rotation platform would have to fulfil several critical requirements. Firstly, the rotation platform would have to be able hold the sample firmly in place during measurement, while still allowing the sample to be reoriented on the horizontal plane. The rotation platform would also need to restrict any unnecessary sample movement in order to ensure the rotation axis of the sample does not change between measurements. In essence, sample would need to be fixed in the rotation plate in such a way that the imaging plane was parallel to the patient bed, causing the same plane to be imaged at all times. Second, the platform and any of its parts would have to be compatible with MRI and not cause any artefacts during measurement. The sample holder could not contain any conductive materials, as the changing magnetic fields present in during MRI would cause the electric currents to be induced in the sample holder. Third, the entire platform assembly would have to fit onto the patient bed of the MRI device and under the body coils used in the measurement.

The final design for the rotation platform shown in Figure 8 consisted of three main components. The base of the platform was a rectangular base plate with angle indicators placed between every 10 degrees. This base plate housed the disk-shaped rotation plate, which in turn contained the sample-holding apparatus. To make sure the sample would not experience

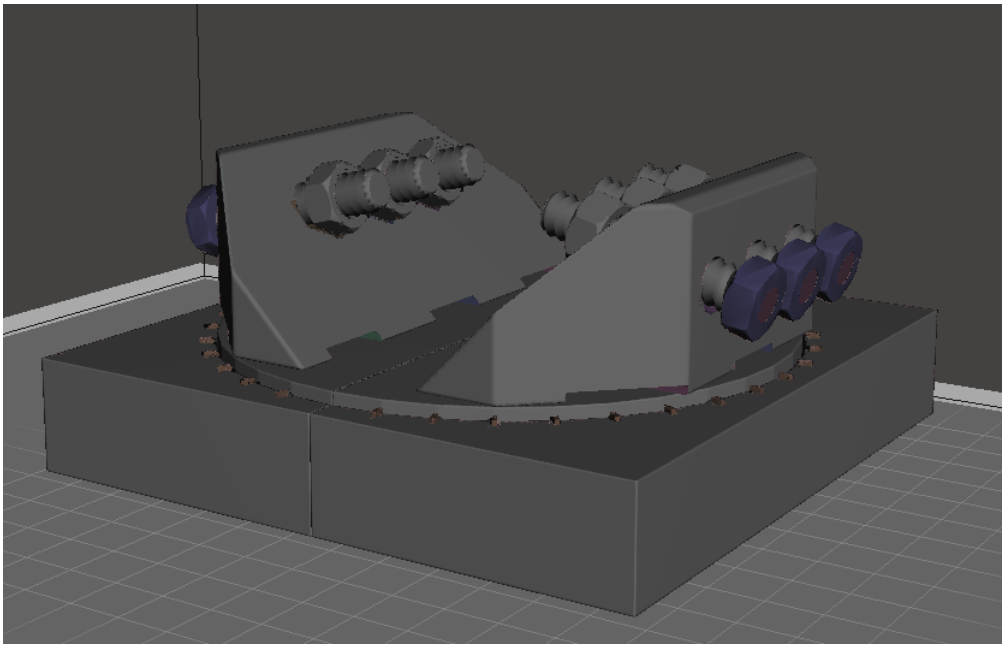

Figure 8: 3D model of the sample rotation platform in its fully assembled configuration. The rectangular base plate houses the circular rotation plate, which in turn serves as a connection point for the slanted sample brace blocks housing the sample fixing screws.

any unwanted motion, it was fixed to the rotation plate using three different methods. Firstly, the sample would be held in place by the two sloped triangular brace blocks. These blocks each contained three adjustable screws, which could be used to further fix the sample in place. Lastly three nylon straps of adjustable length ran around and under the sample to further prevent any unwanted sample movement, the exact placement of which can be seen if Figure 10.

With the exception of the three nylon straps that were bought separately, all of the sample brace parts shown in Figure 9 were 3D printed using an Objet 30 Prime 3D printer at the Oulu University Hospital (OYS) in Oulu, Finland. The platform was printed using an MRI compatible MED610 material. The size of the full platform exceeded the maximum print size of the printer, so the platform had to be printed in parts and assembled later. To help the assembled platform maintain its structure, connector pins and corresponding receptacles were added to the design before printing the parts. The completed platform assembly can be seen in Figure 9.

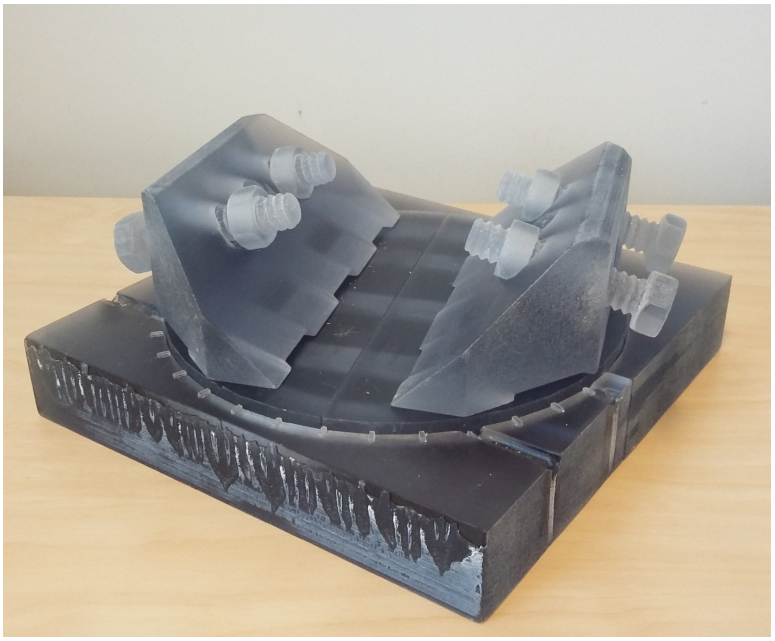

Figure 9: Printed and assembled rotation platform based on the 3D model shown in Figure 8. An error during printing resulted in small deformations on the surface of the base platform. These cosmetic defects had no effect on sample rotation during measurement.

5.2 Measurements

The measurements were performed on a bovine stifle joint. Bovine cartilage was used due to its ready availability and the thickness of the cartilage. In general a bovine joint has thicker cartilage surface compared to human counterparts. This makes the identification of cartilage zones easier, especially when using low field-strength magnets. Previous studies have also shown that the magic-angle phenomenon is present in bovine articular cartilage [1, 3]. The initial joint samples consisted of full length femur and tibia with intact cartilage surfaces on the stifle joint with some remaining soft tissue from the on-site preparation. The samples were bought from Viskaalin farm located in Rova, Muhos.

The joint sample was prepared for measurement by removing excess femoral and tibial bone from the joint, resulting in a 20 cm long, roughly cylindrical sample with a diameter of 14 cm. The prepared sample consisted of the joint and approximately 5 cm long ends of femoral and tibial bone. The femur of the sample was marked during sample preparation to help with sample orientation, placement and identification during measurement. The sample was stored in a freezer (-30 °C) and thawed to room temperature

(21 °C) before measurement. After being thawed, the sample was placed in a vacuum bag and small amount of Dulbecco's phosphate buffered saline (DPBS, Sigma Aldrich), was introduced to the joint capsule. DPBS is a balanced salt solution used in the handling and culturing of mammalian cells. In cartilage samples, DPBS functions both as a pH buffer maintaining the pH of the joint capsule and cartilage surfaces in the physiological range, as well as a way to bring the hydrostatic pressure across the surface of the cartilage sample closer to in vivo conditions. Finally, a vacuum sealer was used to remove any excess air bubbles from the sample bag after which the bag was sealed. The fully prepared sample can be seen in Figure 10.

Figure 10: A bovine stifle join sample placed in the printed rotation platform shown in Figure 9. The sample has been fixed in place on the rotation plate using the sample holding screws and straps.

The MR measurements were done using a 3 T whole body MRI scanner (MAGNETOM Skyra, Siemens Healthcare) at the Oulu University Hospital (OYS) in Oulu, Finland. The imaging sequence used during the measurements was a T_2-weighted multi-echo spin-echo (MESE) sequence with 12 echoes. Before imaging, the base plate of the rotation platform was fixed to the patient bed of the MRI device and the sample was then fixed onto the rotation plate. The sample was positioned on the sample holder (Figure 9) in such a way to simulate a patient laying on the sagittal plane on the patient bed, i.e. the patella of the sample was facing parallel to the surface of the

bed (Figure 10). The initial orientation of the sample was chosen so that the tibia was roughly in parallel to $\mathbf{B}_0$. This orientation was from then on referred to as the zero angle. Twenty slices containing potential areas of interest were selected from the sample. These slices were selected from lateral and medial femoral chondyles, with a split of 8 slices from the medial and 12 from lateral chondyle. Emphasis was placed on obtaining large amounts of intact cartilage from both femur and tibia during slice selection.

The sample rotation and measurement was split into two distinct rotation and measurement sets. The first set consisted of 21 angles ranging from 0 to 200, with a 10 degree rotation between each measurement. For the second set, the sample was brought back to zero angle and rotated 5 degrees. From this new starting point 9 more measurements were taken for angles 5-85, with a 10 degree increment between each measurement. In total the sample was measured at 30 unique orientations. This rotation sequence came about as a compromise between the long measurement time of the MESE sequences, a desire to capture a wide range of angles for the anisotropy analysis, and a need to collect a finer set of data in the interesting 0° to 90° angle range. The measurements used a field of view (FoV) of 199 × 199 mm with a resolution of 768 × 768 pixels, resulting in a pixel size of 0.2604 mm^2. Important measurement parameters have been collected into Table 1.

Table 1: Imaging parameters used with the MESE sequences for determining the T_2 relaxation maps

Echo time (ms)	10.7
Number of echoes	12
Number of slices	20
Resolution (px)	768 × 768
FoV (mm)	199 × 199
Slice thickness (mm)	3
Field strength (T)	3

5.3 Data analysis

Rotating the sample between each measurement has the natural consequence of rotating the resulting MR image as well. This causes the position of the cartilage between each subsequent imaging to shift, meaning that the regions of interest for the cartilage do not overlap. This would lead to every region of interest (ROI) in the imaging sequence to be of different shape and size, making accurate comparison between rotations difficult. In this study, this

Figure 11: T_2 weighted MR image of the slice used during ROI selection at reference angle $\theta = 0$.

problem was alleviated through a process called image coregistration. Image coregistration is the process of aligning the geometries of an image to a reference image with the intention of producing an image that is as similar to the reference image as possible. Image coregistration can use various image transformation and translation techniques, for example translation, rotation, stretching. In this study the images were coregistratered using only translation and rotation. The coregistration was performed using a free license software ELASTIX (version 5.000) [39, 40].

The images created from the T_2-weighted MESE sequences were coregistered to the image taken at 10°. This image was chosen as the reference for both image coregistration and eventual ROI creation, due to its good cartilage contrast. During coregistration it was noted that the software was unable to fully coregister images with orientation differences of over 90° to the reference image. This was solved by manually rotating these images by 90° or 180° before coregistration, in order to better align with the reference image. Using ELASTIX to coregister two images produces a file containing the coregistration parameters that can then be used with TRANSFORMIX,

a supplementary program to ELASTIX, to repeat the image transformation. The first image of each echo train had the strongest signal to noise ratio, and was coregistered to the reference image (10°) using ELASTIX. The remaining echoes of each measurement were then transformed to match these first echoes using TRANSFORMIX. Ideally this would result in the pixels of coregistered images matching those of the reference images perfectly, but the coregistration process does invariably still include small errors due to small changes in the imaging. As seen in Figure 11, the MR images contained a large amount of bone and other non-cartilage tissue in addition to the femoral and tibial cartilage surfaces. These non-cartilage tissues (especially fat and muscle tissue) could not be fixed in place as well as the bone and cartilage surfaces, and as such had a tendency to slightly move during sample rotation. The coregistration of this large amount of slightly shifting non-cartilage tissues was another source of error in coregistration. Additionally images with measurement angles larger than 90° faced initial problems during coregistration, requiring them to be pre-rotated in the clockwise direction by either 90° or 180° before coregistration. To more easily manage the coregistration of the large amount of slices and echoes, a set of Matlab scripts were written to automate the coregistration pipeline.

Of the 20 slices obtained from the MR imaging, a single slice from the lateral chondyle set containing large and intact femoral and tibial cartilage surfaces was chosen for further analysis. To compare the angular dependency of transverse relaxation across different locations of cartilage, 3 separate regions of interest were selected from different parts of the cartilage in the joint. The exact locations of these ROIs are shown in Figure 12. Of the 3 chosen regions 2 were selected from femoral cartilage, one from ventral and one from dorsal side of the joint, with a roughly 90° difference between the cartilage surface orientations. These two ROIs were labelled as FV for ventral and FD for the dorsal ROI. The third ROI was selected from dorsal tibial cartilage, with an approximate 180° difference between cartilage surface orientations with the ventral femoral ROI (FV). This ROI was labelled as TB. The selection process for the three ROIs was performed manually using both the T_2 weighted images and T_2 maps taken and created from the MR images at 10° sample rotation. The two most important features for any potential ROI were the thickness of the cartilage and the straightness of the cartilage surface and bone-cartilage interface, resulting in the creation of rectangular ROIs with similar but as large as possible sizes. Each of the three ROIs were split depth-wise into 2 segments of roughly similar size: a surface segment (SS) containing cartilage mostly from the superficial and transitional zones, and a deep segment (DS) consisting mostly of cartilage from the radial zone.

After image coregistration, the next step in analysis was the creation of

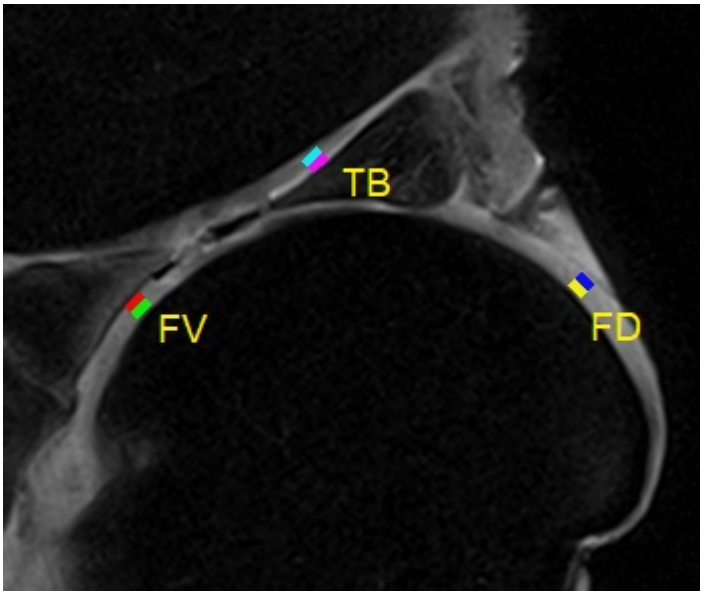

Figure 12: Selected regions of interest and their corresponding labels presented in the reference image used for image coregistration. Each of the selected regions has been further split into two segments shown here in differing colours.

T_2 relaxation time maps for each angle measurement. Two different types of T_2 fits were used in the map generation: a linear and a nonlinear fit equation. For the linear fit, a natural logarithm was taken from the T_2 weighted images, and a linear model of the form

$$\log(S) = \log(S_0) - \mathrm{TE}/T_2 \tag{5.14}$$

was used as the fit function. The nonlinear fitting function, on the other hand, was of the form

$$S = S_0 \exp(-\mathrm{TE}/T_2). \tag{5.15}$$

The nonlinear fitting was performed using the Matlab (R2019b) function fminsearch. The T_2 maps were created by first performing a pixelwise fit using either equation (5.14) or (5.15) on the data given by the echo train of each coregistered MR image. The T_2 values of each individual pixel could then be collected from their corresponding fits and used to create a T_2 map for the selected image. Initially the T_2 fits were performed using the linear fit shown in equation (5.14), which was later replaced by the nonlinear fit function shown in (5.15).

A comparison between the two T_2 maps created using the equations 5.14 & 5.15 can be seen in Figure 13. While the linear fitting process was orders of magnitude faster than the nonlinear fit, it also resulted in a large amount

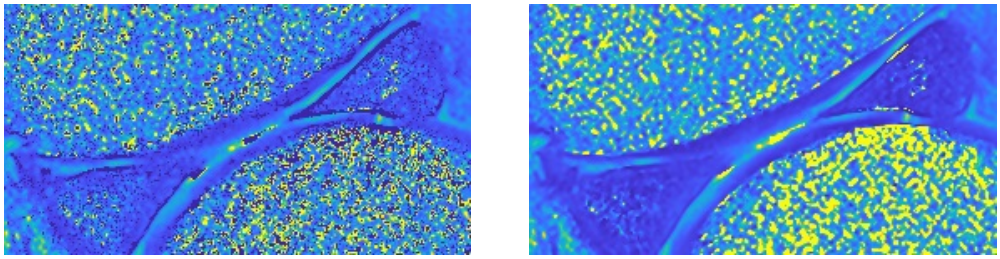

(a) Linear fit **(b)** Nonlinear fit

Figure 13: Comparison between the linear and nonlinear T_2 fits. Incomplete fits are shown in the images as dark blue.

of zero valued pixels in the T_2 maps, especially around cartilage surfaces and at the cartilage-bone interface. These values are caused by a failed fitting defaulting the T_2 value to zero. In Figure 13 these can be seen as the dark blue pixels. The nonlinear fits have a notably fewer number of these zero value pixels, indicating a superior fitting quality compared to the linear fit.

After T_2 map generation, the segmented ROIs were added to the maps and their positions were checked to coincide with the cartilage. Due to the imperfect image coregistration process some of the T_2 maps still displayed an image shift of approximately 1 to 3 pixels. This was addressed by manually adjusting the location of the ROI segments to better match the desired cartilage location. Fitting errors during T_2 calculation caused some of the pixels close to the subchondral bone and cartilage surfaces to display unrealistically high T_2 values, varying from thousands to tens of thousands of ms. By comparison the T_2 values obtained from the center of the cartilage would generally be 0-150 ms. When encountered, the pixels containing these fitting errors were manually omitted from their respective ROIs, consequentially reducing the total pixel count of the affected ROI segment. A cutoff threshold of 300 ms was used for omitting these large T_2 values. The final averaged pixel counts for each segment are presented in Table 2.

The direction of cartilage surfaces in a knee sample is not uniform. The natural curvature of the cartilage surfaces in the femoral and tibial heads of any sufficiently large knee sample causes an orientation difference between the studied region and the reference frame of the sample. Naturally this also causes an initial angle between the assumed collagen fiber orientation and B_0 field to be present, even when the sample is oriented at 'zero angle' to the magnetic field. These initial offsets in ROI orientation were estimated from the MR images using Mokkula, a Matlab based image processing and calculation software developed at the Research Unit of Medical Imaging, Physics and Technology. The estimated offset angles have been collected in

Table 2: Average pixel counts and offset angles of cartilage surface normal orientation for each ROI segment.

ROI	SS Avg px count	DS Avg px count	Offset (deg)
Femur (ventral)	44.9	51.5	40
Femur (dorsal)	45.3	45.7	-54
Tibia	48.9	45.0	19

Table 2.

The transverse relaxation times for each ROI segment were obtained by averaging the T_2 values of each ROI segment of the T_2 maps created for each sample rotation. This resulted in six sets of data each containing 30 averaged T_2 values of an individual ROI segment at different sample orientations. These T_2 values were then converted into the corresponding relaxation rates R_2 and a relaxation anisotropy model was individually fitted to each dataset using a Matlab curve fitting tool. The fitting used for describing the relaxation anisotropy was a modified version of the anisotropy model shown in Equation (4.13) [3, 6]. The modifications to the equation consisted of an offset angle Δ to account for the difference between the estimated and real collagen fiber orientations, and of a normalisation term 1/4 to the anisotropic relaxation component. The final anisotropy model was of the following form:

$$\frac{1}{T_2} = R_2 = R_{2,i} + R_{2,a}(3cos^2(\theta + \Delta) - 1)^2/4 \tag{5.16}$$

The parameters evaluated by the fitting were the isotropic component $R_{2,i}$, the anisotropic component $R_{2,a}$ and the offset term Δ. To assess the quality of the fitted anisotropy model a set of goodness of fit (gof) parameters were also calculated from the fits. The sum of squares due to error (SSE), also known as summed square of residuals, measures the total deviation between the measured values and the values obtained from the fit. It is calculated using the following equation

$$SSE = \sum_{i=1}^{n}(y_i - f(x_i))^2, \tag{5.17}$$

where y_i are the measured values and $f(x_i)$ are the fit values. As the SSE describes the summed square of residual error, an SSE value close to zero indicates the fit functions well at predicting measured values. Root mean squared error (RMSE) is an estimate of the standard deviation of the random component of the data. Also known as fit standard error or standard error

of regression, it is calculated using the following function.

$$RMSE = \sqrt{MSE} = \sqrt{\frac{SSE}{v}}, \tag{5.18}$$

where v is the number of degrees of freedom in the fit, MSE is the mean squared error and SSE is the sum of squares due to error. As with SSE, an RMSE value closer to zero indicates the fit functions well in predicting the measurement values.

6 Results

The MR imaging results collected from the T_2-weighted measurements of the bovine stifle joint have been separated into two parts. The first part examines the results of the plotted R_2 data collected from the three chosen regions of interest, and the anisotropy model fits (Equation 5.16) across all six selected ROI segments.

The second part examines how changing the width of a ROI segment affects the R_2 averaging process, and how this affects the quality of the corresponding anisotropy model fits. For this comparison, three ROI segments of differing size were selected from the same area of articular cartilage and their R_2 plots and corresponding fits using Equation (5.16) were compared.

6.1 Anisotropy of transverse relaxation rate

The transverse relaxation rates (R_2) calculated for each ROI segment with respect to measured sample orientation and the corresponding fits using the anisotropy model (Equation 5.16) have been plotted in Figures 14 - 16. All three Figures show that R_2 values of both surface and deep segments display a clear dependence on the ROI orientation. The effect is especially prominent in the three deep segments. The R_2 values of all three surface segments are without exception lower than the values of their deep segment counterparts at any given measurement point. All of the fits made using the anisotropy model (Equation 5.16) function well in describing their corresponding datasets. In general, the gof parameters for the surface segment fits are better than those of the corresponding deep segment fits, indicating that the quality of the surface segment fits match their respective datasets slightly better than the deep segment fits.

The fitting parameters, minima locations and gof parameters from the fits shown in Figures 14-16 have been stored in Tables 3 and 4. Table 3 contains the parameters of the three surface segment fits, while Table 4 contains the parameters for corresponding the deep segment fits.

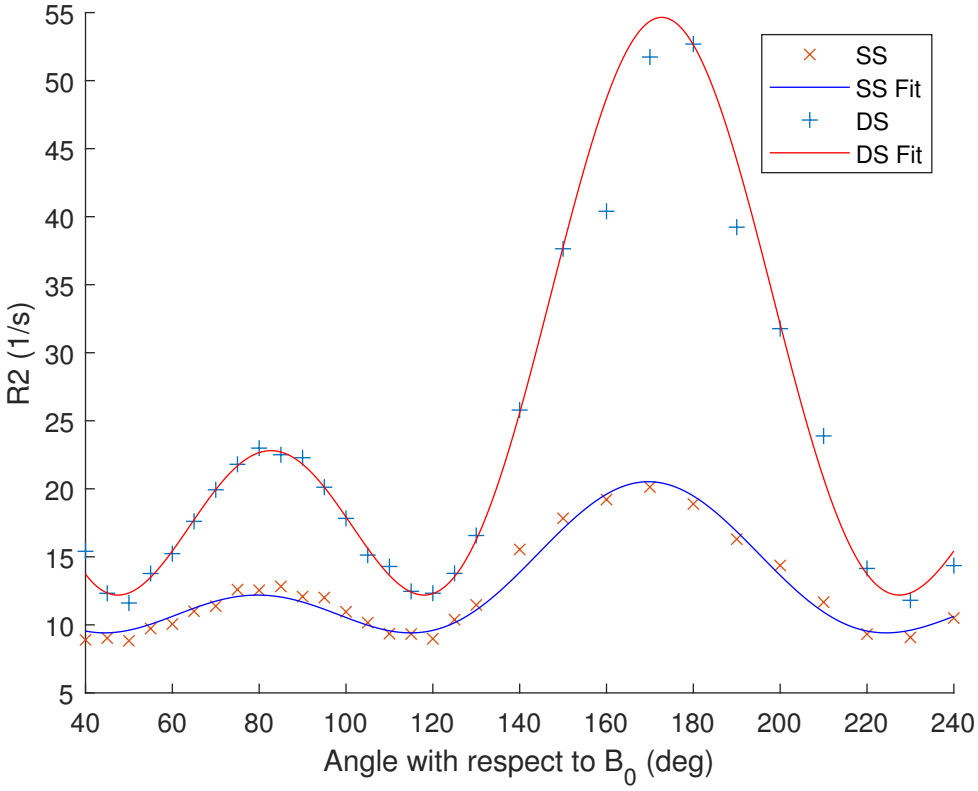

Figure 14: Orientation dependence of the average relaxation rates R_2 for two cartilage segments in the ventral femoral ROI. The angles represent the orientation of the ROI surface normal with respect to B_0. The data was fitted using Eq. (5.16) for both segments separately.

Figure 14 displays the average R_2 values calculated from both segments of the ventral femur ROI as a function of ROI surface normal orientation with respect to B_0. The figure also displays the anisotropy model (Eq. 5.16) fits for both segments. The maximum (54.64) and minimum (12.19) values of the deep segment fit differ by a significant amount, indicating a strong R_2 anisotropy. The difference between maximum (20.52) and minimum (9.41) values of the surface segment fit is also notable, though smaller compared to the one in the deep segment. The fitted model for the surface segment appears to match its respective dataset well at all angles. While the deep segment fit loses some accuracy between angles $160° - 190°$, it too behaves remarkably well, especially between angles $60° - 130°$. The two positive angles where the R_2 values of the fits reach their minimum are 47.5° and 118.8° for the deep segment, and 44.4° and 114.9° for the surface segment.

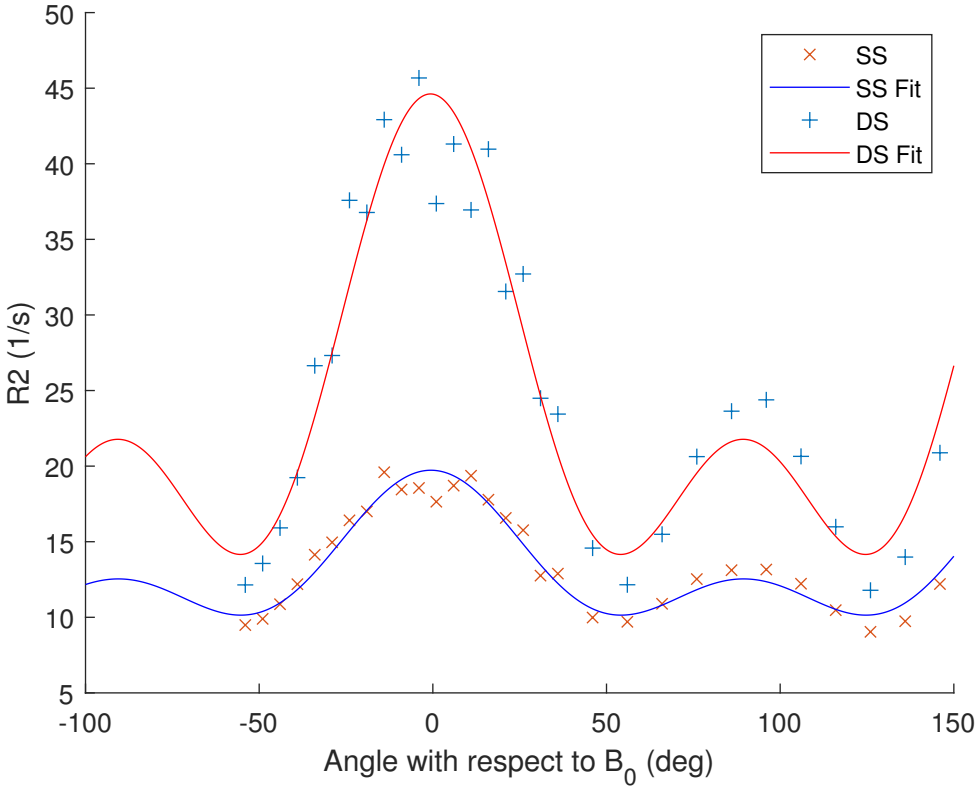

Figure 15: Orientation dependence of the average relaxation rates R_2 for two cartilage segments in the FD ROI. The angles represent the orientation of the ROI surface normal with respect to B_0. The data was fitted using Eq. (5.16) for both segments separately..

Figure 15 displays the average R_2 values calculated from both surface and deep segments of the FD ROI as a function of ROI surface normal orientation with respect to B_0. The difference between the maximum (44.62). and minimum (14.16) R_2 values in the deep segment is smaller than that of FV, indicating a smaller degree of orientation anisotropy present in the ROI. The difference between the maximum (19.73) and minimum (10.15) values of the surface segment fit is again smaller than that of the deep segment. Compared to the results from FV the data from both segments of FD seems to be more noisy, especially at fast R_2 (i.e. fast T_2) rates. The deep segment fit, although noticeably less accurate compared to the corresponding fit of the other femoral ROI FV, still functions well in describing the general form of the anisotropy. The minima locations calculated for both surface segment (54.2° and 124.7°) and deep segment fits (54.1° and 124.6°) are very close the the magic angles.

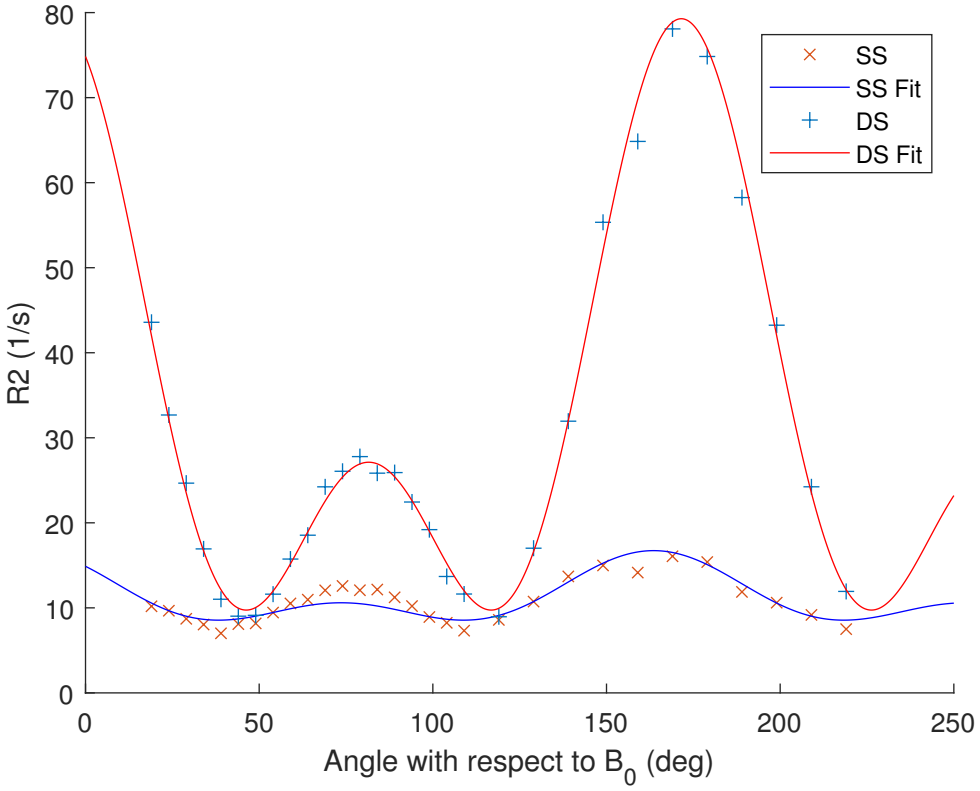

Figure 16: Orientation dependence of the average relaxation rates R_2 for two cartilage segments in the TB ROI. The angles represent the orientation of the ROI surface normal with respect to B_0. The data was fitted using Eq. (5.16) for both segments separately.

Figure 16 displays the average R_2 values calculated from both surface and deep segments of the TB ROI as a function of ROI surface normal orientation with respect to B_0. The difference between maximum (79.28) and minimum (9.75) R_2 values in the deep segment is the largest of the three ROIs by a significant margin. At the same time the difference between the maximum (16.7) and minimum (8.55) values of the surface segment are the smallest of the three ROIs. In general the fit quality in the deep segment appears to be good. The fit for the surface segment is the least accurate of the three surface segment fits with SSE and RMSE values of 34.74 and 1.134 respectively. On visual inspection the surface fit still appears good, although the fit loses some accuracy around angle 80°. The first two positive minima locations for the fitted anisotropy models are 46.3° and 116.8° for the deep segment fit, and 38.3° and 108.8° for the surface segment fit.

Table 3: Fit parameters, minima locations and gof parameters for the surface segment fits. The first four rows display the fitting parameters and locations of the first two minima, followed by the gof parameters calculated from the fits.

	Femur (FV) SS	**Femur (FD) SS**	**Tibia SS**
$R_{2,i}$ **(1/s)**	9.41	10.14	8.55
$R_{2,a}$ **(1/s)**	11.11	9.59	8.18
Δ **(deg)**	10.35	0.56	16.44
Minima angle (deg)	44.4, 114.9	54.2, 124.7	38.3, 108.8
SSE	11.03	22.00	34.74
RMSE	0.639	0.903	1.134

All three surface segment fits display clearly defined isotropic and anisotropic components that vary little between the different cartilage types and orientations of the ROIs. The isotropic and anisotropic components have similar values in all three ROIs, with the largest difference in FV. The values of the offset terms for the surface segment fits show notable variance between the segments. The offset parameter of the Fermur 02 fit is roughly 0.56° degrees, while FV and TB have noticeably larger offset terms of 10.35° and 16.44° degrees. The minima locations of the three fits also correspond reasonably well to those predicted by the anisotropy model, with a roughly 70° difference between the locations of the two subsequent minima. The minima locations of FD in particular are both within one degree of the predicted magic angles. The gof parameters of all three fits indicate that the fits function reasonably well in predicting the anisotropic properties of the R_2 in surface segments. The fit of FV ROI has the best fitting quality with gof parameters of SSE: 11.03 and RMSE: 0.639, while quality of the fit for TB has the lowest with corresponding gof values of SSE: 34.74 and RMSE: 1.134.

Table 4: Fit parameters, minima locations and goodness of fit parameters for the deep segment fits. The first four rows display the fitting parameters and locations of the first two minima, followed by the gof parameters calculated from the fits.

	Femur (FV) DS	**Femur (FD) DS**	**Tibia DS**
$R_{2,i}$ **(1/s)**	12.19	14.16	9.74
$R_{2,a}$ **(1/s)**	42.46	30.46	69.54
Δ **(deg)**	7.28	0.67	8.46
Minima (deg)	47.5, 118.0	54.1, 124.6	46.3, 116.8
SSE	20.52	235.43	47.44
RMSE	0.87	2.95	1.33

Similarly to the surface segment, all three deep segment fits also display clearly defined isotropic and anisotropic components. The values of these parameters vary notably more across the different ROIs than those of the surface segment fits. For example, the value of the anisotropic component of TB is more than double that of FD. The values of the isotropic components ($R_{2,i}$) of the deep segment fits also vary more noticeably across the different ROIs, though not to the same degree as $R_{2,a}$.

The values of the offset terms for the three deep segment fits also show notable differences. The offset term for the FD fit has a value very close to zero at 0.67°. The offset terms for FV and TB are comparatively larger with values of 7.28° and 8.46° respectively. Compared to the offset values in the surface segment fits in Table 3, the offsets of the deep segment fits of FV and TB are smaller than their surface segment counterparts by a change of 3.07° for FV, and 7.98 ∘ for TB. These correspond to reductions of 29.7% and 45.8% between the segments. The offset parameter of FD deep segment on the other hand is slightly larger than that of the surface segment with an increase of 0.09°. Minima locations of the deep segment fits also align well with those predicted by the relaxation anisotropy model, with a roughly 70° difference between the minima. Similarly to the surface segment, the minima locations in FD are very close to the magic angles. The goodness of fit parameters of the three deep segment fits show that the fits function reasonably well in describing the observed anisotropy, though at a reduced accuracy compared to the surface segment fits. Especially the SSE values of the fits are noticeably large when compared to their surface counterparts. The fit quality is the highest in FV, while FD displays the poorest fit quality with a notably high SSE.

6.2 Effect of ROI size on transverse anisotropy

The R_2 values for each ROI segment used in the orientation analysis were obtained by calculating the averaged T_2 values from their corresponding T_2 maps. Thus the amount of pixels in each segment directly affects the calculated R_2 values in two equally important ways. Firstly, increasing the amount of pixels naturally increases the amount of data in the averaging, leading to lower maximum values obtained. Secondly, the only way to reasonably increase the size of a ROI from the cartilage is to widen it. Widening the ROI to contain more cartilage runs the risk of collecting cartilage in different orientations compared to the 'original' ROI orientation, leading to a reduction in the strength of the orientation dependence.

To compare the effect the pixel amount within the segment has on the resulting R_2 values, two additional tibial cartilage ROIs were created. These ROIs were made by selecting the original TB ROI and extending or contracting it along the cartilage surface, while attempting to preserve the original cartilage surface orientation. TB was chosen for the size comparison as the cartilage surface around that ROI was relatively flat, allowing the extension and contraction of the ROI, while still assuming the collagen fiber orientation remains unchanged. The average pixel counts for the deep segments of the three ROIs are: 45 pixels for the original segment, 75 pixels for the doubled segment and 21 pixels for the halved segment.

After ROI generation, the R_2 values for each ROI orientation were calculated from the averaged T_2 values and the anisotropy model (Equation 5.16) was fitted to each of the datasets. Figure 17 shows both the R_2 graphs and the anisotropy model plots of the three deep segment ROIs. The fit and error parameters collected from these three fits are shown in Table 5.

Table 5: Fit and error parameters for the TB deep segment fits made using the halved (21 pixel), original (45 pixel) and doubled (75 pixel) ROIs

	Halved (21px)	**Original (45px)**	**Doubled (75px)**
$R_{2,i}$ **(1/s)**	10.20	9.74	9.47
$R_{2,a}$ **(1/s)**	76.34	69.54	60.60
Δ **(deg)**	9.33	8.46	7.55
SSE	109.44	47.44	31.99
RMSE	2.01	1.326	1.09

Comparing the fitting parameters of the three ROIs in Table 5 reveals that the magnitudes of both the isotropic and anisotropic component decrease as the pixel count of the corresponding ROI increases. The larger segment

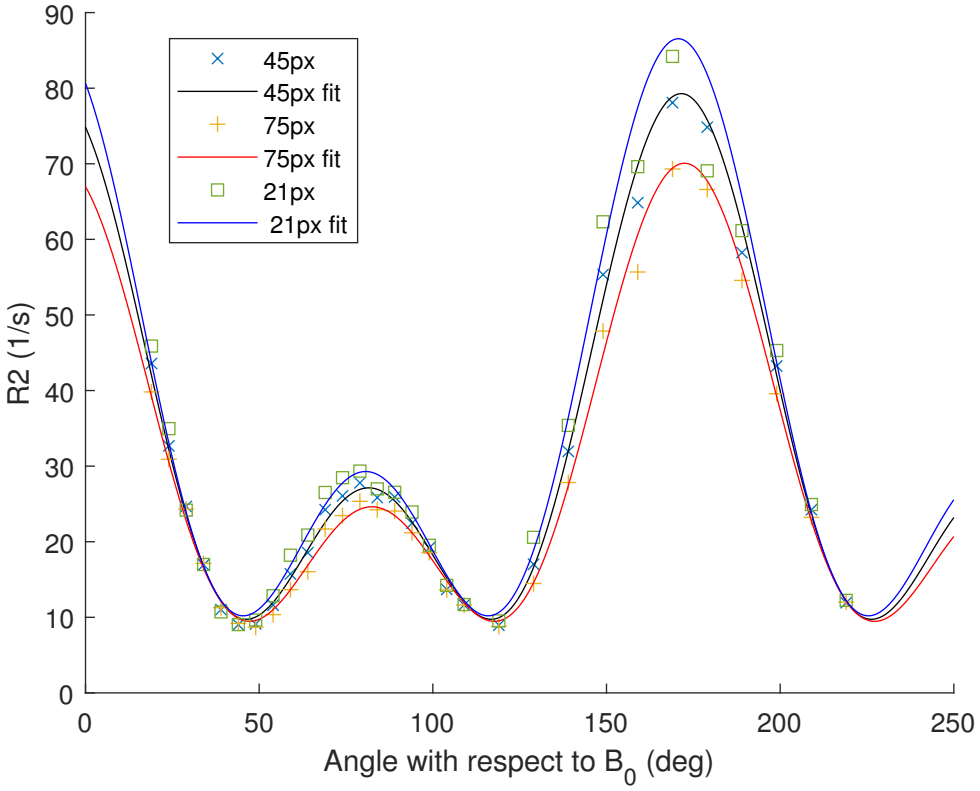

Figure 17: Orientation dependence of the average relaxation rates R_2 for the three TB ROIs of different sizes. The angles represent the orientation of the ROI surface normal with respect to B_0. The data was fitted using Eq. (5.16) for all three segments separately.

displays a lower value for both fitting components, while the smaller segment has increased parameter values for both components compared to the original segment. The change in the anisotropic component can be explained by the larger ROI resulting in the R_2 being averaged over a larger sampling of different fiber orientations. The observed change in the isotropic component is harder to explain, but it is most likely a result of the rations of TZ and RZ changing within the ROIs. The offset parameters Δ also differ between the altered segments and original by ± 1 deg. The goodness of fit parameters of the three fits are also similar. Most notable difference between the three fits is the change in SSE, the value of which increases notably for the smaller segment. The gof parameters for the fits seem to degrade somewhat as the ROI size decreases, while improving slightly for the larger ROI.

7 Discussion & conclusions

The purpose of this work was to study the anisotropy of the transverse relaxation rates R_2 in articular cartilage, and to see if a modified version of a previously used mathematical model [3] could be fitted to describe the detected anisotropy. An additional goal was to study the differences in the orientation dependence of the relaxation parameters in cartilage obtained across different locations within the joint. In this study the analysed ROIs were selected from the cartilage surfaces of femoral and tibial bone ends.

The measurements consisted of magnetic resonance imaging of a bovine stifle joint at multiple different orientations. The joint consisted of an intact patella, femur and tibia each with a fully intact cartilage surface. The T_2 weighted MRI images were used to create T_2 relaxation time maps for a slice containing cartilage from femoral and tibial bone ends. Three regions of interest were selected from the full MRI images, two regions from femur and one from tibia, containing a rectangular selection of cartilage from the surface to the perceived bone-cartilage interface. The relaxation time maps for these three regions were then used to analyse the orientation anisotropy of the cartilage. To accurately reorient the sample between individual measurements, a rotation device compatible with the specifications of a clinical MRI device was designed and created.

The measurement results showed that all six studied ROI segments displayed a notable degree of transverse relaxation anisotropy, the strength of which increased noticeably in the deeper ROI segments. This coincides well with literature findings, as the cartilage from the deeper regions has been shown to exhibit larger degrees of T_2 anisotropy compared to the surface [3, 28, 37, 38, 41]. The detected anisotropy behaved according to the mathematical model used in the study (Equation 5.16).

The strongest angle dependence was found in the three deep segments of the selected ROIs, which all displayed a clear R_2 (and T_2) anisotropy. These findings agreed well with previous knowledge of the structure of articular cartilage, as the bottom 50% of cartilage volume consists mostly of the strongly ordered radial zone and the partially ordered lower parts of the transitional zone. These highly ordered structures are the main causes for the orientation anisotropy of articular cartilage [6]. The large differences in the amplitudes of the anisotropic components in the three deep sections are notable, with the $R_{2,a}$ of TB being over double of FD. This can be explained by the varying thickness of the cartilage in the selected regions resulting in different ratios of TZ and RZ in each ROI. This study was performed without collecting more accurate zonal information of the studied cartilage, usually obtained via f.ex. polarized light microscopy. Due to this, the T_2 maps could not be compared

to histological data describing the cartilage zones in the sample.

While lesser in strength to the anisotropy detected in the deep segments, all three surface segments also displayed a clear T_2 orientation dependence. The surface zone of cartilage forms a region with fiber orientations perpendicular to the cartilage surface normal. Rotating the sample naturally causes the surface zone to also rotate within the magnetic field. This can lead to the zone displaying degree of T_2 anisotropy, especially if there is a bias in the fiber orientations within the surface zone. The resolution used in the study would however have resulted in the data collected from the SZ to be averaged with parts of the underlying TZ, weakening its effect. Depending on the thickness of the transitional and radial zones it is also entirely feasible that the surface segment could contain cartilage from all three structural zones. This means that the detected anisotropic behaviour in the surface segment of the articular cartilage can either be fully caused by the transitional and surface zones, or the segment can also contain some amount of radial zone. In the latter case the strong orientation anisotropy of the radial zone would still only have had a limited impact on the total relaxation anisotropy of the surface segments due of the averaging process used during data analysis.

The results showed that the isotropic components of the deep and surface segment fits of any given ROI displayed relatively little difference between the three ROIs. On the other hand, the anisotropic components experience a large change when going from the SZ/TZ dominated surface segment to the DZ dominated deep segment. Even in the case of FD, the ROI with the smallest difference in $R_{2,a}$ between its two segments, the increase in $R_{2,a}$ value from surface to deep segment was over 3-fold (from 9.59 to 30.46 1/s). This large increase in the anisotropy terms going from SS to DS can be explained by the organisation of the collagen fibers increasing in the deeper segments of the cartilage.

The quality of fit estimates calculated for all six ROI segments are in general better for the surface segment fits compared to their deep segment counterparts. The gof parameters of the deep segment fits are larger than those of their corresponding surface segments, indicating a more imperfect fit. The ranges for the R_2 values in the deep segments (as seen in Figures 14-16) are noticeably larger compared to the surface segments. This makes the fitting process more difficult for the deep segment fits, and is likely the main reason for the observed loss of goodness.

The offset terms of the surface (Table 3) and deep (Table 4) segment fits displayed notable differences between the corresponding segments. This was not wholly unexpected, as the orientation between the bone-cartilage interface and the cartilage surfaces can vary noticeably within an individual ROI. The relatively small pixel size obtained during the imaging also made

defining both of these interfaces challenging. Additionally, the possibility of the orientation of the collagen fibers not being perpendicular to either of these surfaces also exists.

The rotation platform functioned well in both allowing the large sample to rotate between measurements and in preventing any unnecessary sample movement. As the sample rotation was done by hand there will always exist a degree of human error during each rotation. This problem was somewhat alleviated by adding simple angle indicators to the platform. The combined weight of the sample and sample braces resulted in a significant increase in the total mass of the rotation plate during measurements. This proved surprisingly advantageous, as the increased friction between the base and rotation plates helped to prevent any small unintended changes in measurement angle during the removal, adjustment and replacement of the receiver coil between each sample rotation. The sample braces, fixing screws and straps functioned well in keeping the sample in place on the rotation plate during both sample rotation and imaging. As the receiver coil used during measurements was placed directly on top of the sample and the rotation platform, it needed to be lifted up and lowered back down between each sample rotation. A potential way to speed up future measurements would be to devise a scaffold for the receiver coil to rest on, allowing the sample to be rotated without interaction with the coil.

The coregistration of the rotated images functioned well across all measurement angles. The sample was fixed in the rotation plate in such a way that the imaging plane was parallel to the patient bed, causing the same plane to be imaged at all times. Any small human errors during sample fixing and rotation could still have caused the imaging plane to shift slightly between measurements, altering the exact place of the imaging slice within the sample during each rotation. This would naturally cause some small errors in the coregistration process. In this study, the images were coregistered without the use of masking, causing the coregistration program to place equal importance on both cartilage and its surrounding tissues. Although the quality of the coregistration was still deemed acceptable without the use of masking, any further studies using samples with such a large amount of 'extra' tissue would most likely benefit from cartilage masking during coregistration. The resolution of the imaging also has a significant effect in the quality of the coregistration.

The imaging resolution caused the pixels close to the surface and bone-cartilage interface to potentially contain signal from non-cartilage tissues in addition to cartilage. This naturally makes finding the exact locations of the bone-cartilage interface and the cartilage surface more difficult, resulting in the ROIs possibly containing data from outside the cartilage. The relatively

small resolution also made the zonal differentiation of the cartilage infeasible, as the surface zone would most often be thinner than the width of a single pixel. Increasing the resolution of an MRI imaging sequence leads to other drawbacks, such as longer imaging times. Combining the MRI results to a histology study using f.ex polarized light microscopy would give a more accurate representation of the zonal structure of the cartilage.

The amount of pixels used in the T_2 averaging was found to have a relatively small effect on the R_2 values. Increasing the size of the ROI along the cartilage surface lead to a slight decrease in both isotropic and anisotropic fitting parameters, with the most notable changes seen in the anisotropic component. Conversely decreasing the size of the ROI by contracting it lead to an increase in the fitting parameter values. The observed changes in the offset values can be explained by the apparently straight bone-cartilage interface still containing some curvature even along these relatively short distances. This results in the offset terms of each different sized ROI being averages over a different sampling of fiber orientations, resultantly causing their values to differ. Great care must be taken during ROI selection to ensure all selected ROIs are of similar size, in order prevent the differing pixel counts from affecting the analysis results.

This study was done using only a single sample. To improve the reliability of any follow-up study, further measurements would need to be performed using a larger set of samples. Special attention would also need to be placed on ROI selection when using multiple samples in order to ensure the selected cartilage regions remain comparable. Improving the imaging resolution would also allow for better distinction between cartilage zones, especially the surface zone. In this study the sample was rotated along the plane of the patient bed of the MRI device. Performing the sample rotations along multiple axes would allow for a more detailed picture of the anisotropy in three dimensions. Changing the type of sample or the rotation scheme would however require a significant redesigning of both the measurement set up, especially that of the sample rotation platform, and analysis process. In this study the ROIs were selected exclusively from the femoral and tibial bone ends. The patella of the sample was also found to contain a substantial cartilage surface, and could be an interesting candidate for comparative studies in the future.

One of the major goals of T_2 anisotropy studies of articular cartilage is to be able to apply the knowledge gained on the relaxation anisotropy in a clinical setting. The ability to model the anisotropic behaviour of articular cartilage could, for example, be applied in removing the magic angle artefact from clinical images, improving the diagnosis of cartilage condition via MRI. One major milestone towards reaching this goal would be to perform a study similar to the one in this thesis on in vivo human cartilage. In this study, both

the range and number of unique sample angles used during the measurement was notably large, a fact made possible by the wide bore of the clinical MRI device and the design of the rotation platform. This novel combination of a large set of unique angles, use of a full joint sample, and the use of a clinical MRI device hopes to help bridging the gap between the clinical and pure research fields with regards to T_2 relaxation anisotropy. While this study has shown the feasibility of anisotropy measurements using a large sample in a clinical magnet, significant adjustments in the measurement protocol must still be made in order to make in vivo measurements feasible. Notably, the patient would need to remain completely stationary during imaging, a fact made very challenging by the lengths of the imaging sequences. Additionally, while a severed knee sample can be freely rotated in the bore of the magnet, any in vivo measurement of the knee would by necessity have a severely more limited range of motion.

This study proved that the magic angle phenomenon can be detected in articular cartilage using a clinical MRI device, and that the observed T_2 orientation anisotropy behaves according to a previously established mathematical model. The value of these isotropic and isotropic components can be viewed as a indicator of the contribution these mechanisms have on the total relaxation of the sample. In the surface segments these components had similar values, coinciding well with the assumption of a low degree of anisotropy. In the deep segments of cartilage the anisotropic components were 2-7 times larger than isotropic components, indicating an increase of tissue organisation and relaxation anisotropy. In addition to the relaxation anisotropy results, valuable information on both preparation and imaging of large samples using a clinical MRI device was gained during the study. Based on the results of this study, a continuation project has already been started in the MIPT research group at Oulu University. This project aims to expand upon the presented relaxation anisotropy measurements using both a larger number of relaxation parameters and joint samples.

References

[1] N. Hänninen, J. Rautiainen, L. Rieppo, S. Saarakkala, and M. J. Nissi. "Orientation anisotropy of quantitative MRI relaxation parameters in ordered tissue". *Scientific reports* 7.1 (2017), pp. 1–11.

[2] R. M. Henkelman, G. J. Stanisz, J. K. Kim, and M. J. Bronskill. "Anisotropy of NMR properties of tissues". *Magnetic Resonance in Medicine* 32.5 (1994), pp. 592–601.

[3] Y. Xia and K. Momot. *Biophysics and Biochemistry of Cartilage by NMR and MRI*. Royal Society of Chemistry, 2016.

[4] S. Erickson, R. Prost, and M. Timins. "Radiology". *The 'magic angle' Effect: Background physics and clinical relevance* 188.1 (1993), pp. 23–25.

[5] Y. Xia, J. B. Moody, and H. Alhadlaq. "Orientational dependence of T2 relaxation in articular cartilage: A microscopic MRI (μMRI) study". English. *Magnetic resonance in medicine* (2002).

[6] M. Bydder, A. Rahal, G. D. Fullerton, and G. M. Bydder. "The magic angle effect: A source of artifact, determinant of image contrast, and technique for imaging". *Journal of Magnetic Resonance Imaging* 25.2 (2007), pp. 290–300.

[7] A. Borthakur, E. Mellon, S. Niyogi, W. Witschey, J. B. Kneeland, and R. Reddy. "Sodium and T1rho MRI for molecular and diagnostic imaging of articular cartilage". *NMR in Biomedicine* 19.7 (2006), pp. 781–821.

[8] K. I. Momot, J. M. Pope, and R. M. Wellard. "Anisotropy of spin relaxation of water protons in cartilage and tendon". *NMR in Biomedicine* 23.3 (2010), pp. 313–324.

[9] V Mlynárik, P Szomolányi, R Toffanin, F Vittur, and S Trattnig. "Transverse relaxation mechanisms in articular cartilage". *Journal of Magnetic Resonance* Volume 169, Issue 2 (2004), pp. 300–307.

[10] S. Zheng, Y. Xia, and F. Badar. "Further studies on the anisotropic distribution of collagen in articular cartilage by μMRI". *Magnetic Resonance in Medicine* 65.3 (2011), pp. 656–663.

[11] M. T. Nieminen, J. Töyräs, M. Laasanen, S. J. Silvennoinen, H. J. Helminen, and J. S. Jurvelin. "Prediction of biomechanical properties of articular cartilage with quantitative magnetic resonance imaging". *Journal of Biomechanics* 37 (2007), pp. 321–328.

[12] M. Huber. "Anatomy, Biochemistry, and Physiology of Articular Cartilage". *Investigative radiology* (2002).

[13] J. A Buckwalter and H. J Mankin. "Articular cartilage. Part I: Tissue design and chondrocyte-matrix interactions". English. *Journal of bone and joint surgery. American volume* (1997).

[14] A. J. Sophia Fox, A. Bedi, and S. A. Rodeo. "The basic science of articular cartilage: structure, composition, and function". *Sports Health* 1 (2009), pp. 461–468.

[15] A. R. Poole, T. Kojima, T. Yasuda, F. Mwale, M. Kobayashi, and S. Laverty. "Composition and structure of articular cartilage: a template for tissue repair". *Clinical Orthopaedics and Related Research®* 391 (2001), S26–S33.

[16] P Julkunen, R. K. Korhonen, M. J. Nissi, and J. S. Jurvelin. "Mechanical characterization of articular cartilage by combining magnetic resonance imaging and finite-element analysis—a potential functional imaging technique". *Physics in Medicine and Biology* 53.9 (Apr. 2008), pp. 2425–2438.

[17] A. Benninghoff. "Form und Bau der Gelenkknorpel in ihren Beziehungen zur Funktion". *Zeitschrift für Zellforschung und mikroskopische Anatomie* 2.5 (1925), pp. 783–862.

[18] E. T. T. Brown, A. H. A. Damen, and A. Thambyah. "The mechanical significance of the zonally differentiated collagen network of articular cartilage in relation to tissue swelling". *Clinical Biomechanics* 79 (2020), p. 104926.

[19] J. M Clark. "The organization of collagen fibrils in the superficial zones of articular cartilage". English. *Journal of anatomy (Print)* (1990).

[20] R. W. Brown, M. R. Thompson, R. Venkatesan, Y.-C. N. Cheng, and E. M. Haacke. *Magnetic Resonance Imaging : Physical Principles and Sequence Design.* Vol. Second edition. Wiley-Blackwell, 2014.

[21] V. Kuperman. *Magnetic Resonance Imaging : Physical Principles and Applications.* Electromagnetism. Academic Press, 2000.

[22] H. D. Young. *Sears and Zemansky's university physics : with modern physics.* Ed. by H. D. Young. 12th ed. Includes index. San Francisco: Pearson Addison-Wesley, 2007.

[23] M. H. k. Levitt. *Spin dynamics : basics of nuclear magnetic resonance.* Second edition. Hoboken, N.J.: Wiley, 2007.

[24] C. C. Finlay, S. Maus, C. D. Beggan, T. N. Bondar, A. Chambodut, T. A. Chernova, A. Chulliat, V. P. Golovkov, B. Hamilton, M. Hamoudi, R. Holme, G. Hulot, W. Kuang, B. Langlais, V. Lesur, F. J. Lowes, H. Lühr, S. Macmillan, M. Mandea, S. McLean, C. Manoj, M. Menvielle, I. Michaelis, N. Olsen, J. Rauberg, M. Rother, T. J. Sabaka, A. Tangborn, L. Tøffner-Clausen, E. Thébault, A. W. P. Thomson, I. Wardinski, Z. Wei, and T. I. Zvereva. "International Geomagnetic Reference Field: the eleventh generation". *Geophysical Journal International* 183.3 (2010), pp. 1216–1230.

[25] J Hennig. "K-space sampling strategies". *European Radiology* 9 (1999), pp. 1020–1031.

[26] B. Bipin Mehta, S. Coppo, D. Frances McGivney, J. Ian Hamilton, Y. Chen, Y. Jiang, D. Ma, N. Seiberlich, V. Gulani, and M. Alan Griswold. "Magnetic resonance fingerprinting: a technical review". *Magnetic Resonance in Medicine* 81.1 (2019), pp. 25–46.

[27] Y. Jo, J. Kim, C. Park, J. Lee, J. Hur, D. Yang, B. Lee, D. Im, S. Hong, E. Kim, E.-A. Park, P. Kim, and H. S. Yong. "Guideline for Cardiovascular Magnetic Resonance Imaging from the Korean Society of Cardiovascular Imaging—Part 1: Standardized Protocol". *Korean Journal of Radiology* 20 (Sept. 2019), p. 1313.

[28] R. Dibb, L. Xie, H. Wei, and C. Liu. "Magnetic susceptibility anisotropy outside the central nervous system". *NMR in Biomedicine* 30.4 (2017), e3544.

[29] S. J Erickson, I. H Cox, J. S Hyde, G. F Carrera, J. A Strandt, and L. D Estowski. "Effect of tendon orientation on MR imaging signal intensity : a manifestation of the magic angle phenomenon". English. *Radiology* (1991).

[30] H. J. C. Berendsen. "Nuclear Magnetic Resonance Study of Collagen Hydration". *The Journal of Chemical Physics* 36.12 (1962), pp. 3297–3305.

[31] G. D Fullerton, I. L Cameron, and V. A Ord. "Orientation of tendons in the magnetic field and its effect on T2 relaxation times". English. *Radiology* (1985).

[32] M. T. Nieminen, J. Rieppo, J. Töyräs, J. M. Hakumäki, J. Silvennoinen, M. M. Hyttinen, H. J. Helminen, and J. S. Jurvelin. "T2 relaxation reveals spatial collagen architecture in articular cartilage : A comparative quantitative MRI and polarized light microscopic study". English. *Magnetic resonance in medicine* (2001).

[33] S. Peto and P. Gillis. "Fiber-to-field angle dependence of proton nuclear magnetic relaxation in collagen". *Magnetic Resonance Imaging* 8.6 (1990), pp. 705–712.

[34] N. M. Menezes, M. L. Gray, J. R. Hartke, and D. Burstein. "T2 and T1rho MRI in articular cartilage systems". *Magnetic Resonance in Medicine* 51.3 (2004), pp. 503–509.

[35] H. Atkinson, T. Birmingham, R. Moyer, J. Milner, J. Thiessen, R. Thompson, D. Holdsworth, and J. Giffin. "Acute qMRI response of tibiofemoral articular cartilage in participants at risk for knee OA after challenged walking". *Osteoarthritis and Cartilage* 26 (2018). Abstracts from the 2018 OARSI World Congress on Osteoarthritis, S390–S391.

[36] Y. Xia. "Relaxation anisotropy in cartilage by NMR microscopy (μMRI) at 14-μm resolution". *Magnetic Resonance in Medicine* 39.6 (1998), pp. 941–949.

[37] J. E. Kurkijärvi, M. J. Nissi, J. Rieppo, J. Töyräs, I. Kiviranta, M. T. Nieminen, and J. S. Jurvelin. "The zonal architecture of human articular cartilage described by T2 relaxation time in the presence of Gd-DTPA^2". *Magnetic Resonance Imaging* 26 (2008), pp. 602–607.

[38] S. Zheng and Y. Xia. "The collagen fibril structure in the superficial zone of articular cartilage by μMRI". *Osteoarthritis and Cartilage* 17 (2005), pp. 1519–1528.

[39] S. Klein*, M. Staring*, K. Murphy, M. A. Viergever, and J. P. Pluim. "elastix: a toolbox for intensity-based medical image registration". *IEEE Transactions on Medical Imaging* 29.1 (Jan. 2010), pp. 196 –205.

[40] D. P. Shamonin, E. E. Bron, B. P. Lelieveldt, M. Smits, S. Klein, and M. Staring. "Fast Parallel Image Registration on CPU and GPU for Diagnostic Classification of Alzheimer's Disease". *Frontiers in Neuroinformatics* 7.50 (Jan. 2014), pp. 1–15.

[41] L. Wang and R. R. Regatte. "Investigation of regional influence of magic-angle effect on T2 in human articular cartilage with osteoarthritis at 3 T". *Academic radiology* 22.1 (2015), pp. 87–92.